University of Oslo

Master thesis

DFT Calculations of Metal Oxide Semiconductors

An Improvement of Optical and Electronic Property Calculations

Mariel Aulie Hinderaker

May 24, 2022

Abstract

Oxide semiconductors are essential materials in optoelectronics and they will especially be important when we move towards a net-zero gas emission society. Hence, the optical and electronic properties of semiconductor oxides are of great interest. In this thesis the quantum mechanical modeling of semiconductor oxides are evaluated, optimized and discussed. The thesis evaluates different approximations to the exchange correlation functional, different approaches for calculating the high-frequency dielectric constant, the static dielectric constant and the tolerance parameters for convergence of the numerical methods used in the modeling. In addition, the $\boldsymbol{k} \cdot \boldsymbol{p}$ method was implemented in the quantum mechanical modeling software, VASP, in order to improve the accuracy of the calculations. Optical and electronic properties of eight different metal oxides are presented in this thesis. The materials considered are the ε- and β-phase of gallium oxide, the α-quartz modification of silicon dioxide, tin(II)- and tin(IV)-oxide, the rutile and anatase phase of titanium dioxide and wurtzite zinc oxide. This evaluation focuses on the main properties such as crystalline structures, the lattice parameters, the direct and indirect band gap energies, the electronic band structure, the density of states (DOS), the dielectric functions, the absorption coefficients, the static dielectric constant and the high-frequency dielectric constant. The approximation that provided the overall most accurate results were the hybrid functional with an exchange-correlation energy consisting of 30% Hartee-Fock exchange energy and 70% Perdew-Burke-Ernzerhof (PBE) exchange energy. This approximation provided calculated lattice parameters in good agreement with experimental values. For the calculation of the static dielectric constant, a well relaxed structure is significant. Hence, the calculations for this property were performed with the generalized gradient approximation with PBE potential, on a hybrid functional optimized structure. The high-frequency dielectric function is in accordance to the Moss relation inverse proportional to the band gap value of the material considered, which was confirmed by the calculations in this project. Hybrid functional calculations were performed for high-freqency dielectric properties, because they are known to provide accurate bandgap values. The $\boldsymbol{k} \cdot \boldsymbol{p}$ method proved to present insufficient eigenstates when performing this method using a Γ point calculations. However, the $\boldsymbol{k} \cdot \boldsymbol{p}$ method is expected to provide more accurate eigenstates with the use of more reference points.

Sammendrag

Halvlederoksider er essensielle materialer innen optoelektroniske applikasjoner. De vil spesielt være viktige i utviklingen mot det grønne skiftet. Dette gjør at de optiske og elektroniske egenskapene til halvelederoksider er av stor interesse. I denne oppgaven vurderes og optimaliseres den kvantemekaniske modelleringen av halvlederoksider. Forskjellige tilnærminger til exchange-correlation energien, ulike tilnærminger til beregningene av de dielektriske konstantene, og toleransekriteriet for konvergens av numeriske metoder brukt i modelleringen tas i betraktning. I tillegg implementeres $\boldsymbol{k \cdot p}$ metoden i den kvantemekaniske modelleringsprogramvaren, VASP, for å forbedre nøyaktigheten til beregningene. Optiske og elektroniske egenskaper presenteres for åtte forskjellige oksider, nemlig ε- og β-fasen av galliumoksid, α-kvarts modifiseringen av silisiumdioksid, anatas tinnoksid, rutil tinndioksid, rutil- og anatas titandioksid og wurtzite sinkoksid. Evalueringen fokuserer på følgende egenskaper som krystallstrukturer, gitterparametre, båndgapsenergier, elektroniske båndstrukturer, tilstandstettheter, dielektriske funksjoner, absorpsjonskoeffisienter, statiske dielektriske konstanter og høy-frekvens dielektriske konsanter. Tilnærmingen til exchange-correlation energien som ble valgt består av 30 % Hartree-Fock exchange energi og 70 % Perdew-Burke-Ernzerhof (PBE) exchange energi. Denne tilnærmingen resulterte i beregnede gitterkonstanter som samsvarer bra med eksperimentelle verdier. For å beregne den statiske dielektriske konstanten er det nødvendig med en nøye relaksert krystall struktur. Derfor er beregningene for denne egenskapen utført med generalisert gradient tilnærming med PBE potensial, på en allerede hybrid funksjonal relaksert struktur. Høy-frekvens dielectriske konstanter er invers proporsjonale med båndgapenergien til et gitt material, ifølge Moss relasjonen. Dette ble også observert gjennom beregningene. Hybrid funksjonal beregninger ble utført for å beregne høy-frekvens dielektriske egenskaper fordi denne funksjonalen er kjent for å beregne mer nøyaktige båndgapsenergier. $\boldsymbol{k \cdot p}$ metoden viste seg å resultere i utilstrekkelige eigentilstander ved Γ punkt beregninger. Metoden er derimot forventet å gi mer nøyaktige eigentilstander ved bruken av flere referansepunkter i beregningene.

Acknowledgements

Firstly, I would like to express my gratitude and appreciation towards my supervisor, Professor Clas Persson. The completion of this thesis could not have been possible without his helpfulness and his infinite knowledge about materials sciences and quantum mechanics.

The simulations in this thesis were performed by resources provided by Sigma2 - the National Infrastructure for High Performance Computing and Data Storage in Norway. I would like to thank Espen Tangen for helping me out regarding the $\boldsymbol{p}$ matrix generated by VASP.

A debt of gratitude is owed to my parents, Monica H. Aulie and Arve A. Hinderaker, who raised me to believe in science and to be curious of the unknown.

I would like to thank my boyfriend, Kristian S. Lervik, and my sister, Aurora A. Hinderaker, for being good listeners to problems of varying magnitude throughout my studies. Thank you for your support and encouragement.

Last but not least, I would like to thank my classmates, Anna S. Rongve and Benedicte P. Allum, who happens to be my best friends. Because of you, the last two years of the master program have been amazing, even despite the pandemic. I will certainly miss being your classmate.

Contents

Chapter 1

Introduction

Oxide semiconductors are important materials in optoelectronics and they will especially be important when we move towards a net-zero gas emission society. In order to achieve this we need to take advantage of abundant and non-toxic materials. Optical and electronic properties for eight different oxides are presented in this thesis. The materials considered are the ε- and β-phase of gallium oxide, the α-quartz modification of silicon dioxide, tin(II)- and tin(IV)-oxide, the rutile and anatase phase of titanium dioxide and wurtzite zinc oxide.

The optical and electronic properties presented are calculated using first principles density functional theory (DFT). DFT is a widely used tool for quantum mechanical modeling of materials. It is often interesting to have theoretical values to support upon experimental values, which is the intention of the calculations in this work. How a material responds to an applied electrical field is important when considering possible applications in the optical and electronic region. This will be studied closely and compared to experimental values.

DFT is a quantum mechanical approach for modeling materials, and as for quantum mechanics there are still some unresolved questions. The biggest mystery is how electrons in a material effect each other. Or to be more precise, how we can calculate the potential caused by electrons in a material. Therefore, in DFT an ansatz, a guess, for this potential has to be made. There are many good approximations for this potential, resulting in values in agreement with experimental value. However, a property that repeatedly gets incorrectly estimated is the bandgap values. The type of ansatz that will be used in the calculations in this work is known as a hybrid functional potential. This is a potential that has proven to yield bandgap values in good agreement with experimental values. There are different hybrid functional potential and some of these will be tested in order to find out which one will be best suited for this work.

Another problem when it comes to calculating semiconductors is due to the integration method used in the numerical calculations. In quantum physics and in DFT the properties of the electrons are described by wavefunctions. The properties of the electrons and therefore also the material are found by solving the Schrödinger equation in the reciprocal space. This will be described more in detail in Sect. 2.2.6. For calculating electronic and optical properties with density functional theory (DFT) one has to integrate over the reciprocal space. For semiconductors it is the tetrahedron method. This method is based on linear interpolation, which therefore is dependent on small step sizes to give sufficient approximations, especially near the valence band maximum (VBM) and the conduction band minimum (CBM) because of the curvature of the bands. With the intention to illuminate this problem, optical properties near the parabolic bands will be considered and discussed.

In stead of solving the Schrödinger equation for each point in the reciprocal space to find the energies, the energies at only one point can be exploited as a basis set and used to calculate the energies for all the points in the reciprocal space considered. This method is known as the $\boldsymbol{k \cdot p}$ method and is reported to be more time efficient than the "regular" method. It is a well known method in semiconductor physics, but it is not well used within DFT yet. Hence, the intention of this thesis is also to implement this method in Vienna ab initio simulation package (VASP), the tool used for DFT calculations.

Chapter 2

Theory

2.1 Materials

2.1.1 Semiconductors

The energies accessible to individual electrons in a crystalline material are described by continuous functions known as energy bands [33]. These energy bands are of allowed energies, separated by regions of forbidden energies [14], called the bandgap. The collection of occupied electronic states at 0 K is called the valence band and the collection of unoccupied states at 0 K is called the conduction band. The band filling is in accordance to the Pauli exclusion principle. If one or two bands are partly filled at 0 K the material is a semiconductor. When exposed to an applied field the electrons may be excited from the valence band to the conduction band, resulting in electronic conduction. Their response to such an applied field will be considered in this project. In accordance to the Fermi-Dirac distribution the probability for occupancy in the conduction bands increase with increasing temperature. The electronic conduction is therefore also affected by the temperature.

Wide Bandgap Semiconductors

High-power switching devices for upcoming renewable energy are vital for the green shift. Wide-bandgap semiconductors are promising materials in this area due to their high breakdown field [34]. Their wide bandgap provides unique properties, including the ability to absorb and emit light in the ultraviolet (UV) region. This makes them highly suitable for UV light emitting devices, detectors and laser diodes [17].

Another important challenge regarding how to perform the green shift is concerning abundance. Several of the oxides considered in this work are highly abundant materials. In addition to their potential in the optoelectronic region, they also have potential in regions such as water, food, and dermatology.

The materials studied in this work are wide-bandgap semiconductors and some of them are even ultra-wide bandgap semiconductors. A material with ultra-wide bandgap is defined as a material with a bandgap larger than 4 eV, while a bandgap bigger than 3 eV is defined as a wide bandgap [33]. In this chapter the materials studied in this work are presented.

Zinc Oxide

Zinc oxide exists in three main crystal structures, wurtzite, zinc blende and rock salt. Zinc oxide crystallized in the wurtzite structure, w-ZnO, is the most thermodynamically stable phase and will be considered in this project.

Zinc oxide is an earth abundant, low-cost, transparent wide-band semiconductor. It has potential concerning the optoelectronic field, such as for laser diodes and light-emitting diodes in the ultraviolet region [26]. It is already used in applications such as piezoelectric transducers, optical waveguides, conductive gas sensors, and transparent conductive electrodes [27]. Among non-electronic applications, it is widely used in cosmetics, paint, ceramics, sunscreen, etc [11].

2.1.2 Silicon Dioxide

To this day there are nine known allotropic modifications of silicon dioxide [3]. This project will focus on the crystalline quartz modification of silica, α-SiO_2, which is the most important and the most abundant silica mineral.

Silicon dioxide, also known as silica is a very abundant semiconductor material. 90% of the Earth's crust consists in fact of silica. With this kind of access to the material, it is natural that silica has been used since the beginning of the human timeline. The range of areas of use are in in glass, ceramics, tools and jewelry, among others. Today the use of silica has extended to the solar cell industry and high-tech applications such as optical devices, quantum technology and piezo quartz [15]. All though it is an insulator, it is also important in the semiconductor field.

Titanium Dioxide

Titanium dioxide exists in six known phases, whereas four of these occur naturally [38]. These faces are known as brookite, TiO_2 (B), rutile and anatase. This project will concern the rutile phase and the anatase phase of TiO_2, denoted as r-TiO_2 and a-TiO_2 respectively. Both of these are stable at most temperatures, however, the rutile phase is the most stable in macroscopic sizes and anatase is the most stable in nanoscopic sizes [29]. The anatase phase is the preferred polymorph in the case of solar cell applications [38].

TiO_2 is attractive in photocatalysis, because of its efficient photoactivity, high stability, and low cost. It is significant in transparent electronic devices, for example; thin films, sensors, and transistors. It also has high hydrophilicity, making it useful for self-cleaning coatings.

Tin Oxide

Tin oxide exists in two major variants. Both of these variants, tin(II) oxide, and tin(IV) oxide, will be considered in this project. Tin(II) oxide crystallizes in an anatase structure, while tin(IV) oxide crystallizes in an rutile structure. Hence, they will be denoted respectively as a-SnO and r-SnO_2 further in this work.

The majority of the research concerning tin oxide is based on r-SnO_2 due to its wide bandgap. This property has made the variant attractive and important in optoelectronic technologies such as in gas sensors, thin-film transistors, photovoltaic cells, etc. [35].

Limited research are available on a-SnO. This is because of its tendency to undergo disproportionation at a specific temperature and pressure [35]. However, due to the variant's potential to be used in thermoelectric generators and solar cells, research performed on this variant is increasing. a-SnO has potential for applications including oxide electronics and thermoelectrics. a-SnO could be a good replacement for other thermoelectric materials, since the predominant thermoelectric materials are unstable at higher temperatures and are either toxic or have deficient access. a-SnO is among the oxide thermoelectrics that is earth-abundant and non-toxic [1].

Gallium Oxide

Gallium oxide is a transparent, ultra-wide band-gap semiconductor that is very attractive in optoelectronics, as solar cells, solar-blind UV photodetectors, and gas sensing devices. It can occur in five different phases. These are denoted as α, β, γ, δ and ε. A transient phase denoted as κ has also been reported and is often mixed with the ε-phase. The present work will provide calculated properties regarding β- and ε-phases of gallium oxide, β- and ε-Ga_2O_3.

β-gallium oxide has been studied more comprehensive than the other phases, because it is the most thermodynamically stable phase. However, because of its strong anisotropy it is interesting to study for other phases as well.

One of the phases crystallizes into an orthorhombic structure with space group Pna_2. In the reported literature it has been designated as both κ and ε. The phase it is mistaken with crystallizes in a hexagonal structure, with the space group $P6_3mc$. The κ and ε phases have very similar structures. The hexagonal phase is constructed by the twinning of three rotational domains of the orthorhombic phase [37]. The ε-polymorph denoted in this work will refer to the orthorhombic structure.

2.2 The Density Functional Theory

The calculations in this thesis are based on first-principles density functional theory (DFT) in conjunction with the Kohn-Sham equation. Due to its computational efficiency and accuracy, this theory is the most widely used electronic structure method. It is used for diverse modeling problems in various fields of engineering, including material sciences.

DFT describes the ground-state properties of a material by knowing the ground-state electron density. Normally, to analyze the properties of a material, it is necessary to solve the time-independent many-particle Schrödinger equation (neglecting spin for simplicity),

$$H^{en}\Psi^{en}(\boldsymbol{r}, R) = E^{en}\Psi^{en}(\boldsymbol{r}, R). \tag{2.1}$$

Where the Hamiltonian H^{en}, the wavefunction $\Psi^{en}(\boldsymbol{r}, \boldsymbol{R})$, and the total energy E^{en} describe a many-particle system, with en denoting electrons and nuclei.

There are several approximations within DFT. One important approximation is the Born-Oppenheimer approximation (BOA), which divides the nuclei (n) and the electrons (e) into separate mathematical problems. The many-particle wavefunction, $\Psi^{en}(\boldsymbol{r}, \boldsymbol{R})$, describes all the electrons and nuclei and is simplified by variable separation into an electron part, $\Psi(\boldsymbol{r})$, and a nuclei part, $\Theta(\boldsymbol{R})$. The many-particle Schrödinger equation is thereby simplified to the electronic Schrödinger equation,

$$H\Psi(\boldsymbol{r}) = E\Psi(\boldsymbol{r}), \tag{2.2}$$

with $H = H^e$ being the electronic Hamiltonian and E describing the total energy of the electrons. By using BOA it is possible to avoid solving the Schrödinger equation for electrons and nuclei simultaneously. Another challenge occurs regarding the Hamiltonian H. H is a single-electron operator, which should operate on single-electron wavefunctions. The wavefunction $\Psi(\boldsymbol{r})$ is a many-electron wavefunction and how to express it in terms of single-electron wavefunctions $\psi_i(\boldsymbol{r})$ is not yet known. DFT approaches this problem by using the electron density in the system. The theory states that all ground state properties of the material are determined directly from the ground state density,

$$n_0(\boldsymbol{r}) = |\Psi(\boldsymbol{r})|. \tag{2.3}$$

DFT rests on the theorem stating this. This density is found by an iterative self-consistency method which will be described more in detail in Sect. 2.2.2. The theorem was proved by Kohn and Hohenberg and states:

"The ground-state energy from Schrödinger's equation is a unique functional of the electron density." [33]

DFT rests on two fundamental mathematical theorems. The second theorem is based on a set of equations derived by Kohn and Sham:

"The electron density that minimizes the energy of the overall functional is the true electron density corresponding to the full solution of the Schrödinger equation."[33]

A variational principle for the energy density functional states that $E[n_0] < E[n]$, given that n is not the ground-state density.

2.2.1 The Kohn-Sham Equation

If the exact ground state density $n_0(\boldsymbol{r})$ is known, then DFT states that the exact ground state total energy $E[n_0]$ is also known. But the expression of the energy functional $E[n_0]$ is not yet resolved. This DFT problem can instead be solved by the Kohn-Sham equation, a method for finding the exact ground-state density, and thereby also the exact corresponding total energy.

The Kohn-Sham method approximates $\Psi(\boldsymbol{r})$ as a product of individual single electron wave functions,

$$\Psi(\boldsymbol{r}_1, r_2, ..., r_{N_e}) = \psi_1^{KS}(\boldsymbol{r}_1)\psi_2^{KS}(\boldsymbol{r}_2)...\psi_{Ne}^{KS}(\boldsymbol{r}_{N_e}). \tag{2.4}$$

known as a Hartree-like wavefunction. These auxiliary wavefunctions will generate exact electron density depsite the fact that they are not the correct single-electron wavefunctions. N_e is the number of electrons. The density given by these auxiliary wavefunctions is then

$$n(\boldsymbol{r}) = \sum_{j=1}^{N_e} |\psi_j^{KS}(\boldsymbol{r})|^2. \tag{2.5}$$

To find this density one needs to solve the Kohn-Sham equation

$$\{-\frac{\hbar^2 \bigtriangledown^2}{2m_e} + V_H(\boldsymbol{r}) + V_{en}(\boldsymbol{r}) + V_{xc}(\boldsymbol{r})\}\psi_j^{KS}(\boldsymbol{r}) = \varepsilon_j^{KS}\psi_j^{KS}(\boldsymbol{r}). \tag{2.6}$$

Here the terms on the left side is respectively the electron kinetic energy, the Hartree potential $V_H(\boldsymbol{r})$, the electron-nuclei interaction $V_{en}(\boldsymbol{r})$, and the exchange-correlation potential V_{XC}. The right side of Eq. 2.6 consist of the j:th single-particle wavefunction and its corresponding eigenvalue ε_j^{KS}.

The exact total energy as a functional of the exact density in DFT is described by

$$E[n] = F[n] + \int V_{en}(\boldsymbol{r})dr = T[n] + U_{ee}[n] + U_{en}[n], \tag{2.7}$$

consisting of the many-electron systems kinetic energy $T[n]$, the many-electron interaction energy $U_{ee}[n]$, and the many-electron-nuclei interaction $U_{en}[n]$. $T[n]$ and $U_{ee}[n]$ are not yet known. To get around these obstacles, known functionals can be added to the energy equation

$$E[n] = T_s[n] + U_s[n] + U_{en}[n] + \underbrace{\{(T[n] - T_s[n]) + (U_{ee}[n] - U_s[n])\}}_{E_{xc}[n]}. \tag{2.8}$$

While $T_s[n]$, the kinetic energy of the wavefunction, $U_s[n]$, the interaction energy of the wavefunction, and $U_{en}[n]$ can be calculated exactly, the remaining terms cannot. The remaining terms can be treated as one functional, which is known as the exchange-correlation energy: $E_{xc}[n] = (T[n] - T_s[n]) + (U_{ee}[n] - U_s[n])$. The exact total energy of a many-electron system is according to the Kohn-Sham method described by

$$E[n] = T_s[n] + U_s[n] + U_{en}[n] + E_{xc}[n]. \tag{2.9}$$

This expression is exact if $E_{xc}[n]$ is exact. Regardless of an exact ground state density and thereby also an exact ground state total energy, the ground state energy eigenvalues of the Kohn-Sham Hamiltonian however, cannot be exact. This is because the Kohn-Sham auxiliary wavefunctions are not the correct single-particle wavefunctions to the Hamiltonian described in Eq. 2.6. An exact expression for the exchange-correlation functional will never the less give an exact expression for the total energy. This is because the exchange-correlation energy is meant to compensate for the error due to the untrue wavefunction.

As the expression for $E_{xc}[n]$ is unknown, a good approximation is required to approach the total energy of the system, defined in Eq. 2.9.

2.2.2 Self-consistency

The Hartree potential in Eq. 2.6 is defined as

$$V_H(\boldsymbol{r}) = e^2 \int \frac{n(\boldsymbol{r}')}{|\boldsymbol{r} - \boldsymbol{r}'|} d^3\boldsymbol{r}', \tag{2.10}$$

where e is the electron charge and n is the electron density. The Hartree potential is required in order to calculate the electron density. However, we need the electron density in order to know the Hartree potential. This is solved by an iterative method. First an initial guess is made for the electron density $n(\boldsymbol{r})$. Then this density is used to solve the Kohn-Sham equation and to find the single-particle wave functions $\psi(\boldsymbol{r})$. These wavefunctions are used to calculate the electron density $n^{KS}(\boldsymbol{r})$, and finally, the initial density is compared with the calculated density [33]. If the densities are equal, then this is the ground state density. If not, however, the algorithm continues until the ground state density is found. The algorithm is summarized as followed:

1. Initial guess for the electron density $n(\boldsymbol{r})$
2. Find the single-particle wave functions $\psi(\boldsymbol{r})$
3. Calculate the electron density $n^{KS}(\boldsymbol{r})$
4. Compare $n(\boldsymbol{r})$ and $n^{KS}(\boldsymbol{r})$

2.2.3 VASP

Vienna ab initio simulation package, VASP, is a software package for performing first-principles ab-initio quantum-mechanical calculations of crystalline materials using the PAW-method and plane-wave basis set [22, 20, 21]. It calculates an approximation to the many-body Schrödinger equation. This can be done either within density functional theory by solving Kohn-Sham equations or within Hartree-Fock approximation, solving Roothan equations. In this project the hybrid functional will be utilized, which is a combination of Hartree-Fock and Kohn-Sham.

2.2.4 WIEN2k

VASP was used for mostly all the calculations performed in this work. However, the implementation of the $\boldsymbol{k} \cdot \boldsymbol{p}$ method involved some challenges concerning the $\boldsymbol{p}$ matrix, which will be explained more in detail in Sect. 4.5. A solution to this problem was to use WIEN2k to provide corresponding $\boldsymbol{p}$ matrices. WIEN2k is also a software package for performing quantum mechanical calculations [4], but has a basis set of full-potential (linearized) augmented plane waves.

2.2.5 Pseudopotential

The use of pseudopotential instead of exact potentials is among the most important contributions to reducing the computational cost. To simplify the many-electron problem, valence electrons and inner-core electrons are treated separately. This is a valid approximation for most cases because the binding properties are almost solely determined by the valence electrons in semiconductors.

A pseudopotential method is divided into two different approximations, the all-electron calculations, and the frozen core approximation. For the latter, the pseudopotential is used to replace the electron density from the core electrons with a smoothed density. This density is pre-calculated for the core electrons and is "frozen", fixed, in all subsequent calculations. Among the frozen core approximations are the use of ultra-soft pseudopotential (USPP) and the projector-augmented-wave (PAW) method. The latter was introduced by Blöchl and further adapted by Kresse and Joubert for plane-wave calculations [33].

2.2.6 Crystalline Materials

The materials considered in this project are crystalline materials, for which periodicity can be exploited for the calculations. For each material, one can describe a primitive unit cell that can be repeated in all directions of the crystal. The primitive unit cell is spanned by the primitive lattice vectors $\boldsymbol{a_1}$, $\boldsymbol{a_2}$ and $\boldsymbol{a_3}$ and the lattice vectors in real space are defined as

$$\boldsymbol{R} = n_1\boldsymbol{a_1} + n_2\boldsymbol{a_2} + n_3\boldsymbol{a_3}, \tag{2.11}$$

for any positive integer n_1, n_2 and n_3. The potential in a perfect crystal is periodic, $V(r) = V(r+R)$, and thereby the Hamiltonian, H, too is periodic. This means that the periodicity also applies to the electron density $n(r)$. For a system with periodic potential the solution of the Schrödinger equation can be described in terms of the Bloch function,

$$\psi_{\boldsymbol{k}}(\boldsymbol{r}) = e^{i\boldsymbol{k}\cdot\boldsymbol{r}}u_{\boldsymbol{k}}(\boldsymbol{r}), \tag{2.12}$$

which is periodic in space. Solutions of this form are called plane waves. Many of the mathematical problems within DFT are more convenient to solve in terms of $\boldsymbol{k}$, rather than in terms of $\boldsymbol{r}$. Any vector in the continuous reciprocal space can be described as

$$\boldsymbol{k} = m_1\boldsymbol{b_1} + m_2\boldsymbol{b_2} + m_3\boldsymbol{b_3}, \tag{2.13}$$

for any real numbers m_1, m_2 and m_3. The primitive reciprocal lattice vectors $\boldsymbol{b_1}$, $\boldsymbol{b_2}$ and $\boldsymbol{b_3}$ are given by

$$\boldsymbol{b_1} = \frac{2\pi}{\Omega}\boldsymbol{a_2}\times\boldsymbol{a_3}, \qquad \boldsymbol{b_2} = \frac{2\pi}{\Omega}\boldsymbol{a_3}\times\boldsymbol{a_1}, \qquad \boldsymbol{b_3} = \frac{2\pi}{\Omega}\boldsymbol{a_1}\times\boldsymbol{a_2}, \tag{2.14}$$

and $\Omega = \boldsymbol{a_1}\cdot\boldsymbol{a_2}\times\boldsymbol{a_3}$. The reciprocal lattice vectors are defined as

$$\boldsymbol{G} = v_1\boldsymbol{b_1} + v_2\boldsymbol{b_2} + v_3\boldsymbol{b_3}, \tag{2.15}$$

for any positive integer v_1, v_2 and v_3. The Blöch function is periodic in space, meaning that $u_{\boldsymbol{k}}(\boldsymbol{r}) = u_{\boldsymbol{k}}(\boldsymbol{r}+\boldsymbol{G})$. Because of the periodicity, the Blöch function can also be described as

$$u_{\boldsymbol{k}}(\boldsymbol{r}) = \sum_{\boldsymbol{G}} u_{\boldsymbol{k}+\boldsymbol{G}}e^{i\cdot\boldsymbol{G}\cdot\boldsymbol{r}}. \tag{2.16}$$

The solution to the Schrödinger equation at one single $\boldsymbol{k}$ point a summation over all the possible reciprocal lattice vectors G has to be evaluated. This offers computational resource problems. The plane waves have kinetic energy in the form of

$$E = \frac{\hbar^2}{2m}|\boldsymbol{k}+\boldsymbol{G}|^2. \tag{2.17}$$

The energy is expected to be more significant at the lowest energies [33]. Hence, the higher energies can be cut off, and the size of the plane-wave basis set is limited to energies below

$$E_{cut} = \frac{\hbar^2}{2m}G_{cut}^2. \tag{2.18}$$

The given energy cutoff lifts the computational resource problem and limits the summation to plane waves with kinetic energies less than the energy cutoff. The Blöch function is thereby given by

$$u_{\boldsymbol{k}}(\boldsymbol{r}) = \sum_{|\boldsymbol{G}+\boldsymbol{k}|<G_{cut}} u_{\boldsymbol{k}+\boldsymbol{G}}e^{i\cdot\boldsymbol{G}\cdot\boldsymbol{r}}. \tag{2.19}$$

The primitive cell defined by the primitive reciprocal lattice vectors in the reciprocal space is called the Brillouin zone (BZ) [33]. When performing DFT calculations it is the BZ that is integrated over, with integrals of the form

$$\overline{g} = \frac{\Omega}{(2\pi)^3}\int_{BZ} g(\boldsymbol{k})d\boldsymbol{k}. \tag{2.20}$$

The numerical methods for solving an integral of this type yields more accurate results with a higher amount of $\boldsymbol{k}$ points. But they usually converge to the exact results for a certain amount of points. Convergence tests will be performed considering both $\boldsymbol{k}$ points and energy cutoff before starting with the calculations.

This project involves band structure calculations, and high symmetry $\boldsymbol{k}$ points will therefore be of use. A high symmetry $\boldsymbol{k}$ point in the Brillouin zone has site symmetry containing at least one point symmetry operation, which is different from the symmetry of the neighboring $\boldsymbol{k}$ points [31].

Integrals of this form can be evaluated numerically and there are several methods for doing so. The method used for BZ integration for the calculations in this work is the tetrahedron method since it is recommended for calculations with semiconductors. The tetrahedron method uses a finite set of discrete $\boldsymbol{k}$ points to divide the irreducible BZ into several tetrahedra, with a $\boldsymbol{k}$ point in each corner of the tetrahedra. Thereby the tetrahedra fill the whole reciprocal space [33]. Linear interpolation is used to obtain the remaining unknown values within each tetrahedron. Assuming that the function to be integrated over is known at the discrete $\boldsymbol{k}$ points, the integration over the remaining values can also be calculated [5].

2.2.7 The $\boldsymbol{k \cdot p}$ Method

One of the main limitations concerning DFT calculations is the computational time. For achieving more accurate results this requires a higher number of $\boldsymbol{k}$ points to integrate over, and an increase in $\boldsymbol{k}$ points will increase the computational time. A more efficient method for integrating over the Brillouin zone has been developed, which is called the full-band $\boldsymbol{k \cdot p}$ method. It is not based on a newly discovered theory, as it has been used for 70 years already in semiconductor physics. However, it has not yet been normalized in DFT calculations. In DFT, one solves the single-particle Kohn-Sham equation for every single $\boldsymbol{k}$ point in the Brillouin zone. With the $\boldsymbol{k \cdot p}$ method, on the other hand, one only needs to solve the single-particle Kohn-Sham equation for a few reference $\boldsymbol{k}$ points. These reference $\boldsymbol{k}$ points will further be noted as $\boldsymbol{k}_0$ points. The single-particle Kohn-Sham equation is first solved for the reference points in order to find their corresponding eigenvalues, $E_{\boldsymbol{k}_0}$. The wave functions and the energy eigenvalues at other points than the reference points are then calculated by using the $\boldsymbol{k}_0$ eigenvalues as a basis set. This method is extremely time-efficient compared to the traditional way [28].

Luttinger and Kohn [7] introduced a set of auxiliary functions,

$$\chi_j(\boldsymbol{k}, \boldsymbol{r}) = e^{i(\boldsymbol{k}-\boldsymbol{k}_0)\cdot\boldsymbol{r}}\psi_j(\boldsymbol{k}_0, \boldsymbol{r}), \tag{2.21}$$

which is useful in deriving this method. They fulfill the orthonormality conditions

$$\int \chi^*_{j'}(\boldsymbol{k'}, \boldsymbol{r})\chi_j(\boldsymbol{k}, \boldsymbol{r})d^3r = \delta_{j'j}\delta(\boldsymbol{k'} - \boldsymbol{k}), \qquad \sum_j \int \chi^*_j(\boldsymbol{k}, \boldsymbol{r'})\chi_j(\boldsymbol{k}, \boldsymbol{r})d^3k = \delta(\boldsymbol{r'} - \boldsymbol{r}). \tag{2.22}$$

This derivation is described even more in detail by Callaways [7]. The unknown wavefunction $\psi_n(\boldsymbol{k}, \boldsymbol{r})$ is expanded into the known auxiliary functions $\chi_j(\boldsymbol{k}, \boldsymbol{r})$ as

$$\psi_n(\boldsymbol{k}, \boldsymbol{r}) = \sum_j A_{nj}(\boldsymbol{k})\chi_j(\boldsymbol{k}, \boldsymbol{r}) = \sum_j A_{nj}(\boldsymbol{k})e^{i(\boldsymbol{k}-\boldsymbol{k}_0)\cdot\boldsymbol{r}}\psi_j(\boldsymbol{k}_0, \boldsymbol{r}). \tag{2.23}$$

Then one must solve the Schrödinger equation,

$$[\frac{\boldsymbol{p}^2}{2m} + V(\boldsymbol{r})]\psi_n(\boldsymbol{k}, \boldsymbol{r}) = E_n(\boldsymbol{k})\psi_n(\boldsymbol{k}, \boldsymbol{r}). \tag{2.24}$$

Inserting 2.23 into 2.24 gives:

$$\sum_j A_{nj}(\boldsymbol{k})[\frac{\boldsymbol{p}^2}{2m} + V(\boldsymbol{r})]e^{i(\boldsymbol{k}-\boldsymbol{k}_0)\cdot\boldsymbol{r}}\psi_j(\boldsymbol{k}_0, \boldsymbol{r})$$

$$= e^{i(\boldsymbol{k}-\boldsymbol{k}_0)\cdot\boldsymbol{r}} \sum_j A_{nj}(\boldsymbol{k})[E_j(\boldsymbol{k}_0) + (\frac{\hbar}{m})(\boldsymbol{k} - \boldsymbol{k}_0)\cdot\boldsymbol{p} + (\frac{\hbar^2}{2m})(\boldsymbol{k} - \boldsymbol{k}_0)^2]\psi_j(\boldsymbol{k}_0, \boldsymbol{r})$$

$$= E_n(\boldsymbol{k})e^{i(\boldsymbol{k}-\boldsymbol{k}_0)\cdot\boldsymbol{r}} \sum_j A_{nj}(\boldsymbol{k})\psi_j(\boldsymbol{k_0}, \boldsymbol{r})$$

$$\sum_j A_{nj}(\boldsymbol{k})[E_j(\boldsymbol{k}_0) + (\frac{\hbar}{m})(\boldsymbol{k} - \boldsymbol{k}_0)\cdot\boldsymbol{p} + (\frac{\hbar}{2m})(\boldsymbol{k} - \boldsymbol{k}_0)^2]\psi_j(\boldsymbol{k}_0, \boldsymbol{r})$$

$$= E_n(\boldsymbol{k}) \sum_j A_{nj}(\boldsymbol{k})\psi_j(\boldsymbol{k}_0, \boldsymbol{r}).$$

Multiplying with $\psi^*_l(\boldsymbol{k}, \boldsymbol{r})$ and integrating over the reciprocal space, Ω, gives

$$\sum_j A_{nj}(\boldsymbol{k})\{[E_j(\boldsymbol{k}_0 - E_n(\boldsymbol{k})(\frac{\hbar^2}{2m})(\boldsymbol{k} - \boldsymbol{k}_0)^2]\delta_{jl} + (\frac{\hbar}{m})(\boldsymbol{k} - \boldsymbol{k}_0)\cdot\boldsymbol{p}_{lj}\} = 0,$$

where

$$\boldsymbol{p}_{lj} = [\frac{(2\pi)^3}{\Omega}] \int_\Omega d^3r\psi^*_l(\boldsymbol{k}_0, \boldsymbol{r})\boldsymbol{p}\psi_j(\boldsymbol{k}_0, \boldsymbol{r})d^3r.$$

$\boldsymbol{p_{lj}}$ represents the matrix elements of the momentum operator. A non-trivial solution of these simultaneous, linear, homogeneous equations requires the determinant of the coefficients to be zero,

$$H_{jl} - E_n(\boldsymbol{k})\delta_{jl} = 0,$$

$$H_{jl} = [E_j(\boldsymbol{k}_0) + (\frac{\hbar^2}{2m})(\boldsymbol{k}^2 - \boldsymbol{k}_0^2)]\delta_{jl} + (\frac{\hbar}{m})(\boldsymbol{k} - \boldsymbol{k}_0) \cdot \boldsymbol{p}_{lj}. \tag{2.25}$$

$E_n(\boldsymbol{k})$ is obtained by matrix diagonalization.

The accuracy of the calculated properties of a material increases with the increase in the size of the reciprocal space they are calculated over. The full-band $\boldsymbol{k} \cdot \boldsymbol{p}$ method provides a possibility to calculate the properties of a material within a large reciprocal space using much less computational time compared to regular integration methods.

2.3 Optical Properties

2.3.1 Dielectric Functions

The dielectric function is an important property of a material and is also related to optical absorption and electric conductivity. It describes the electronic response of a crystal to an electromagnetic field [19]. The dielectric function consists of a real part and an imaginary part [13],

$$\epsilon(\omega) = \epsilon^{(1)}(\omega) + i\epsilon^{(2)}(\omega). \tag{2.26}$$

This is a simplification, where the local field effects are neglected. From the Kramers-Kronig relations, when the imaginary part of the dielectric function,

$$\epsilon^{(2)}_{\alpha\beta}(\omega) = \frac{4\pi^2 e^2}{\Omega} lim_{\boldsymbol{q}\to 0} \frac{1}{\boldsymbol{q}^2} \sum_{c,v,k} 2w_{\boldsymbol{k}} \delta(\epsilon_{c\boldsymbol{k}} - \epsilon_{v\boldsymbol{k}} - \omega) \times \langle \mu_{c\boldsymbol{k}+e_\alpha \boldsymbol{q}} | \mu_{v\boldsymbol{k}} \rangle \langle \mu_{v\boldsymbol{k}} | \mu_{c\boldsymbol{k}+e_\beta \boldsymbol{q}} \rangle, \tag{2.27}$$

is known, one can calculate the real part,

$$\epsilon^{(1)}_{\alpha\beta}(\omega) = 1 + \frac{2}{\pi} P \int_0^\infty \frac{\epsilon^{(2)}_{\alpha\beta}(\omega')\omega'}{\omega'^2 - \omega^2 + i\eta} d\omega'. \tag{2.28}$$

In these equations describing the dielectric function e stands for the electron charge, Ω is the primitive cell volume, v and c are respectively the valence and conducting band, α and β are cartesian directions, and e_α and e_β are unit vectors. μ_{vk} represents the periodicity in the Bloch wave function and w_k is the weight of $\boldsymbol{k}$ points. In this work the high frequency dielectric constants will also be considered, which are the values of $\epsilon^{(1)}(\omega)$ and $i\epsilon^{(2)}(\omega)$ at $\omega = 0$. For a material the high frequency dielectric constants are inverse related to the materials bandgap described by the Moss relation [30],

$$\epsilon(\omega) = \frac{A}{E_g^2}. \tag{2.29}$$

2.3.2 Absorption

The absorption coefficient, defined in Eq. 2.30, is determined from the dielectric function,

$$\alpha_{\alpha\beta}(\omega) = \frac{2\omega k_{\alpha\beta}(\omega)}{c}, \tag{2.30}$$

$$k_{\alpha\beta}(\omega) = \sqrt{\frac{|\epsilon_{\alpha\beta}(\omega)| - Re\epsilon_{\alpha\beta}(\omega)}{2}}. \tag{2.31}$$

The electronic function is sensitively dependent on the electronic band structure of the crystal [19]. Hence, the arguments regarding error due to linear interpolation are also very accurate concerning the approximation of the dielectric function. This also affects the absorption coefficient, since it is completely dependent on the dielectric function, as shown in Eq. 2.30 and Eq. 2.31. The imaginary part of the dielectric function can also be written in terms of the effective mass, showing a direct context to the curvature of the bands [10],

$$\epsilon^{(2)}_{\alpha\beta}(\omega) = (\frac{4\pi e}{m\omega})^2 |\langle v|p|c\rangle|^2 \rho_{cv}(\hbar\omega)[f(E_v) - f(E_c)], \tag{2.32}$$

where $|\langle v|p|c\rangle|$ couples states with the same electron wave vector in the valence and conduction bands, $\rho_{cv}(\hbar\omega)$ is the joint density of states and $[f(E_v) - f(E_c)]$ is the Fermi functions.

Chapter 3

Computational Details

3.1 Exchange Correlation Functional

To determine which approximation to the exchange-correlation functional would be the best in this project, properties for the different materials were calculated using four different approximations. The properties were calculated based on the generalized gradient approximation (GGA), one with only the Perdew-Burke-Ernzerhof (PBE) functional describing the exchange-correlation potential and the others based on hybrid functionals, which combines Hartree-Fock (HF) energy and PBE energy. The PBE functional is described by the exchange-correlation functional of the local electron density, $n(r)$, and the gradient in the electron density, $\nabla n(r)$,

$$V_{xc}^{GGA}(r) = V_{XC}[n(r), \nabla n(r)]. \tag{3.1}$$

For the hybrid functionals, the factor α specifies the amount of HF exchange energy in a hybrid functional, as described in Eq. 3.2, [23, 16]. The different approximations for α were 0.0, 0.25, 0.30 and 0.375.

$$E_{xc}^{\alpha} = \alpha E_x^{HF} + (1-\alpha)E_x^{PBE} + E_c^{PBE}, \tag{3.2}$$

where E_{xc}^{α} is the total exchange-correlation energy, αE_x^{HF} is the fraction of HF energy, $(1-\alpha)E_x^{PBE}$ is the fraction of PBE energy, and E_c^{PBE} is the PBE correlation energy. $\alpha = 0.0$ is pure PBE exchange correlation energy, $\alpha = 0.25$ is standard and recommended [23], and α =0.375 is commonly used for w-ZnO calculations [16]. Because $\alpha = 0.25$ resulted in many underestimated values and $\alpha = 0.375$ resulted in many overestimated values, $\alpha = 0.3$ was also considered.

The properties calculated for the materials are the lattice parameters a and c (see Table 3.1) and the bandgap (Table 3.2). The results naturally vary with the materials and the properties, but the chosen fraction of the HF energy gives an overall good approach. More emphasis was placed on the lattice constants, rather than the bandgap values, due to the known problem within DFT regarding bandgap and the fact that the Kohn-Sham eigenvalues may not refer to exact single-electron energies.

As illustrated in the data in Table 3.1 the PBE calculations overestimate the lattice parameters slightly. A trend is evident where the lattice parameters decrease as the fraction of HF exchange energy in the exchange-correlation energy increases. An opposite trend is seen in Table 3.2 regarding the bandgap values, where the results increase along with the increase in HF exchange energy.

By comparing the calculated values with experimental values I decided to proceed with $\alpha = 0.3$, exchange-correlation energy consisting of 30% HF exchange energy and 70% PBE exchange energy. This is the approximation which is referred to whenever a hybrid functional calculation is mentioned further in this work. All further calculations presented in this thesis are based on this unless otherwise stated. Whenever a PBE calculation is mentioned in the text, it refers to a GGA calculation with PBE energy.

Table 3.1: Lattice parameters a and c in Å. The calculated values provided by the use of different approximations to the exchange energy in addition to experimental values (Exp) are listed. The different approximations are denoted with different α-values, which specifies the amount of HF exchange energy in the hybrid functional calculation.

		α				
		0.0	0.25	0.3	0.375	Exp
w-ZnO	a	3.29	3.26	3.25	3.25	3.25[f]
	c	5.29	5.23	5.22	5.20	5.21[f]
α-SiO_2	a	5.02	4.97	4.97	4.95	4.913[a]
	c	5.51	5.45	5.45	5.44	5.404[a]
a-TiO_2	a	3.82	3.79	3.79	3.78	3.7842[c]
	c	9.69	9.61	9.60	9.57	9.5146[c]
r-TiO_2	a	4.66	4.61	4.60	4.58	4.594[c]
	c	2.97	2.96	2.96	2.95	2.9581[c]
a-SnO	a	3.87	3.80	3.79	3.77	3.81[b]
	c	5.06	5.00	4.97	4.94	4.84[b]
r-SnO_2	a	4.83	4.76	4.74	4.73	4.74[e]
	c	3.24	3.19	3.19	3.17	3.19[e]
β-Ga_2O_3	a	12.45	12.02	12.02	11.96	12.23[d]
	c	5.88	5.83	5.80	5.80	5.798[d]
ε-Ga_2O_3	a	5.13	5.04	5.03	5.01	5.046[g]
	c	9.42	9.29	9.27	9.24	9.283[g]

[a]Reference [3]
[b]Reference [35]
[c]Reference [29]
[d]Reference [25]
[e]Reference [32]
[f]Reference [12]
[g]Reference [18]

Table 3.2: Optical bandgap energy in the unit eV for each material. The calculated values provided by different approximations to the exchange energy in addition to experimental values (Exp) are listed. The different approximations are denoted with different α-values, which specifies the amount of HF exchange energy in the hybrid functional calculation.

	α				
	0.0	0.25	0.3	0.375	Exp
w-ZnO	0.71	2.48	2.86	3.43	3.4[f]
α-SiO_2	5.71	7.76	8.16	8.79	9.1[a]
a-TiO_2	1.94	3.42	3.74	4.25	3.20[c]
r-TiO_2	1.64	3.12	3.45	3.96	3.0[c]
a-SnO	1.92	2.66	2.82	3.07	2.8 [b]
r-SnO_2	0.63	2.91	3.37	4.11	3.6[e]
β-Ga_2O_3	1.98	4.15	4.53	5.31	4.85 $\pm$0.1[d]
ε-Ga_2O_3	2.05	4.39	4.74	5.45	-

[a]Reference [3]
[b]Reference [35]
[c]Reference [29]
[d]Reference [25]
[e]Reference [32]
[f]Reference [12]

3.2 Convergence Tests

In order to perform numerically converged DFT calculations, it is important to check the numerical convergence for certain properties. This was done for the static dielectric constant ε_0, the high-frequency dielectric constant ε_∞ and the relative energy E_{Rel} respectively in two different ways. The first set of tests was calculated with respect to the cutoff energy and the second set of tests was calculated with respect to the $\boldsymbol{k}$ mesh. The significant convergence is of the relative energy, but I thought it would be interesting to look at the convergence for ε_0 and ε_∞ as well, since these properties will be calculated in this work. The convergence tests were done with PBE calculations. The relative energy, E_{Rel}, calculations were done by comparing two slightly different configurations of the unit cell of w-ZnO. The difference between these configurations was a small displacement in the position for one of the atoms in the unit cell. A systematic numerical error is expected because of the numerical integration method used in the Brillouin zone sampling. However, these systematic numerical errors are cancelled when two structural similar configurations are compared, because the errors are expected to be equal.

The material w-ZnO was chosen for the convergence tests, because it is known to be a challenging material. One would assume that the parameters chosen from the convergence tests of w-ZnO are sufficient for all the materials.

Energy Cutoff

The convergence criterion for the energy cutoff in this thesis is set to be

$$\frac{\Delta E_{\text{Rel}}}{\Delta E_{\text{Cutoff}}} < \frac{1\text{meV}}{50\text{eV}}, \tag{3.3}$$

where E_{Rel} is the relative energy and E_{Cutoff} is the energy cutoff. The requirement is already achieved with 250 eV in energy cutoff as shown in Table 3.3 and Fig. 3.1a. For the dielectric functions ε_{ion} and ε_∞ on the other hand, seen in Fig. 3.1b and Fig. 3.1c, there are severe differences in the resulting values in the energy range 200 to 300 eV. For the dielectric constants the numerical convergences are achieved within approximately 400 eV.

The default energy cutoff for oxygen is 400 eV. This value is larger than the respective energy cutoff for the cations silicon, tin, titanium, gallium, and zinc. Hence, if one were to choose the cutoff energy without convergence tests, 400 eV would be a good choice. Regarding the relative energy, only 250 eV should be sufficient. However, the severe non-convergence for the dielectric constants in this energy region is unfortunate as these are the properties of interest in this thesis. Hence, an energy cutoff of 400 eV will be used for the calculations in this work.

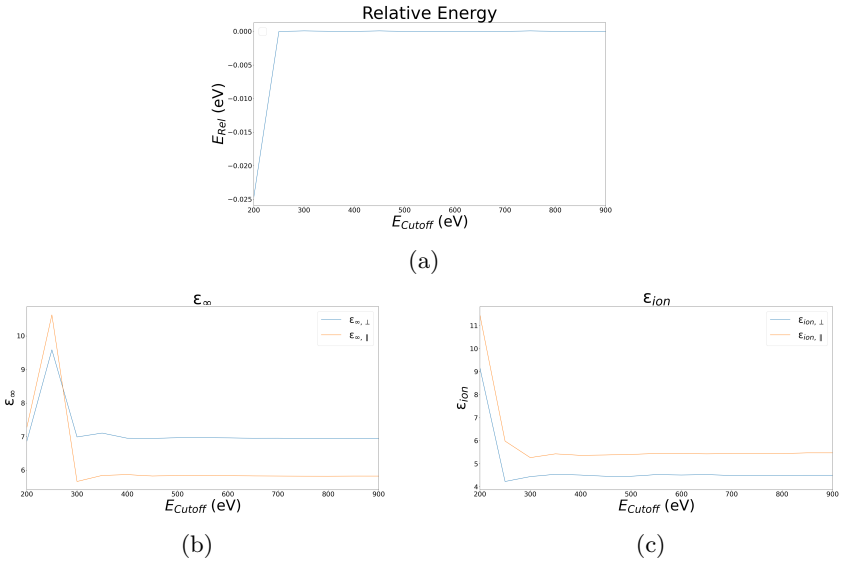

Figure 3.1: (a) The relative energy per unit cell, (b) the high-frequency dielectric constant and (c) the ionic part of the static dielectric constant, all with respect to the energy cutoff.

E_{Cutoff}	E_{Rel}	ΔE_{Rel}	$\varepsilon_{\infty,\perp}$	$\varepsilon_{\infty,\parallel}$	$\varepsilon_{\text{ion},\perp}$	$\varepsilon_{\text{ion},\parallel}$
200	-24×10^{-3}		6.85	7.26	9.17	11.46
250	-9×10^{-6}	2×10^{-4}	9.59	10.63	4.23	5.98
300	8×10^{-5}	9×10^{-5}	6.99	5.66	4.44	5.27
350	2×10^{-5}	-6×10^{-5}	7.11	5.84	4.54	5.43
400	3×10^{-6}	-1×10^{-5}	6.95	5.87	4.51	5.36
450	8×10^{-5}	7×10^{-5}	6.94	5.83	4.46	5.38
500	0.0	-8×10^{-5}	6.97	5.84	4.46	5.41
550	0.0	0.0	6.97	5.84	4.53	5.45
600	0.0	0.0	6.96	5.84	4.51	5.44
650	0.0	0.0	6.95	5.83	4.53	5.43
700	2×10^{-6}	2×10^{-6}	6.95	5.82	4.49	5.44
750	8×10^{-5}	8×10^{-5}	6.94	5.82	4.49	5.44
800	9×10^{-6}	-7×10^{-5}	6.94	5.82	4.49	5.44
850	-3×10^{-6}	-1×10^{-5}	6.94	5.82	4.50	5.47
900	-9×10^{-6}	-1×10^{-5}	6.94	5.82	4.50	5.47

Table 3.3: Relative energy, E_{Rel}, the difference in relative energy, ΔE_{Rel}, the transverse and longitudinal components of the static dielectric constant ε_0 and the high-frequency dielectric constant ε_∞ with respect to the energy cutoff, E_{Cutoff}, all in units of eV. ΔE_{Rel} is between E_{Rel} at the specific E_{Cutoff} and the E_{Rel} at the previous cutoff energy listed in the table. Hence, the empty space for ΔE_{Rel} at E_{Cutoff}=200 eV.

$\boldsymbol{k}$ Space

The requirement for convergence with respect to $\boldsymbol{k}$ points in this thesis is set to be

$$\frac{\Delta E_{\text{Rel}}}{\Delta N_k} < \frac{1\text{meV}}{2}, \tag{3.4}$$

E_{Rel} is the relative energy and N_k is the number of $\boldsymbol{k}$ points along each direction. A $\boldsymbol{k}$ mesh with $M = 4$ obtains relative energies converged within 0.5 meV. However, when using $M > 16$ the convergence is not as expected. For the dielectric constants, there are big differences in the M region of 2 to 8. The longitudinal high frequency dielectric constant $\varepsilon_{\infty,\perp}$ is approximately four times larger at $M = 2$ compared to the value at $M = 8$, as seen in Table 3.4. It is obvious that even though $M = 4$ is sufficient considering the relative energy, a $\boldsymbol{k}$ mesh of this M value will result in deficient dielectric constants. A $\boldsymbol{k}$ grid with $M = 10$ satisfies the requirements for convergence, as illustrated in Fig. 3.2b and Fig. 3.2c. Hence, the structure relaxations will be done by integrating over a $\boldsymbol{k}$ space of $M \times M \times M$ with $M = 4$, while the calculations of the dielectric constants will be done with $M = 10$. The unit cell of ε-Ga_2O_3 includes a number of 40 atoms, which is a much higher number of atoms compared to the other materials considered in this thesis. w-ZnO, for instance, has a unit cell of four atoms. Hence, it is reasonable to believe that the properties for ε-Ga_2O_3 are well converged within a less amount of $\boldsymbol{k}$ points. This is also true β-Ga_2O_3, consisting of 10 atoms in its unit cell. For the hybrid functional calculations of the high-frequency dielectric functions were performed with a $\boldsymbol{k}$ mesh of $8 \times 8 \times 8$ for β-Ga_2O_3 and a $\boldsymbol{k}$ mesh of $6 \times 6 \times 6$ for ε-Ga_2O_3. The DOS calculations were performed with a $\boldsymbol{k}$ mesh of $4 \times 4 \times 4$ for both materials.

M	E_{Rel}	ΔE_{Rel}	$\varepsilon_{\infty,\perp}$	$\varepsilon_{\infty,\parallel}$	$\varepsilon_{\text{ion},\perp}$	$\varepsilon_{\text{ion},\parallel}$
2	6.7×10^{-4}		22.13	16.13	5.18	6.94
4	2.3×10^{-4}	-4×10^{-4}	6.95	5.86	4.51	5.40
6	2.2×10^{-4}	-3×10^{-5}	5.59	5.09	4.43	5.20
8	1.9×10^{-4}	-2×10^{-5}	5.25	4.98	4.43	5.18
10	1.9×10^{-4}	-9×10^{-6}	5.14	5.01	4.43	5.17
12	2.1×10^{-4}	-2×10^{-5}	5.10	5.04	4.40	5.16
14	2.0×10^{-4}	-1×10^{-5}	5.09	5.07	4.40	5.16
16	1.9×10^{-4}	-7×10^{-6}	5.10	5.10	4.40	5.16
18	2.8×10^{-3}	3×10^{-3}	5.10	5.12	4.40	5.16
20	-6.2×10^{-3}	-9×10^{-3}	5.10	5.13	4.40	5.15

Table 3.4: Relative energy, E_{Rel}, and difference in relative energy, ΔE_{Rel}, the transverse and longitudinal components of the static dielectric constant ε_0 and the high-frequency dielectric constant ε_∞ with respect to M, in a $M \times M \times M$ $\boldsymbol{k}$ mesh. The units of E_{Rel} and ΔE_{Rel} are eV. ΔE_{Rel} is between E_{Rel} at the specific $\boldsymbol{k}$ mesh and E_{Rel} at the previous $\boldsymbol{k}$ mesh listed in the table. Hence, the empty space for ΔE_{Rel} at M=2.

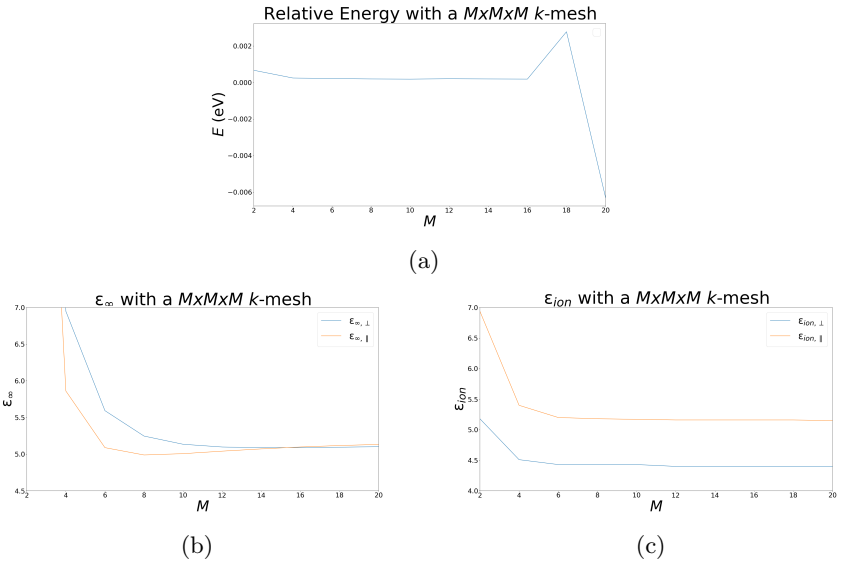

Figure 3.2: (a) The relative energy per unit cell, (b) the high-frequency dielectric constant and (c) the ionic part of the static dielectric constant, all with respect to M, in a $M \times M \times M$ $\boldsymbol{k}$ mesh.

3.3 Static Dielectric Function

The static dielectric constant is expressed as

$$\varepsilon_0 = \varepsilon_{ion} + \varepsilon_\infty. \tag{3.5}$$

In this work the high frequency dielectric constant ε_∞ is calculated by neglecting local field effects. One way to add the ionic contribution is to do a separate calculation using density functional perturbation theory. However, this is not supported for hybrid functional calculations. Therefore, the local field effects were calculated with PBE.

Approaches to the Static Dielectric Constant

Since I already established that $\alpha = 0.3$ calculations provides the best lattice parameters, I wanted to investigate whether or not a mixture of a $\alpha = 0.3$ relaxed structure and a $\alpha = 0.0$ static calculation might give better results than the use of a full $\alpha = 0.0$ calculation. In addition I wanted to see if the use of $\alpha = 0.3$ or $\alpha = 0.0$ provides a more accurate high frequency dielectric constant ε_∞. Three different approximations were calculated for w-ZnO:

PBE: ε_∞ calculated with $\alpha = 0.0$ and ε_{ion} calculated with $\alpha = 0.0$ on an $\alpha = 0.0$ relaxed structure.

PBE-mix: ε_∞ calculated with $\alpha = 0.3$ and ε_{ion} calculated with $\alpha = 0.0$ on an $\alpha = 0.0$ relaxed structure.

HF-mix: ε_∞ calculated with $\alpha = 0.3$ and ε_{ion} calculated with $\alpha = 0.0$ on an $\alpha = 0.3$ relaxed structure.

The different approximations are presented in Table 3.5, which reveals that the HSE-mix yields the best results compared to the experimental values. Therefore, this is the approximation that was used for all the materials in this thesis.

Table 3.5: Dielectric constants of w-ZnO calculated using different approximations.

	PBE	PBE-mix	HSE-mix	Exp
$\varepsilon_{\infty,\perp}$	5.29	3.23	3.23	3.70[a]
$\varepsilon_{\infty,\parallel}$	5.12	3.26	3.26	3.75[a]
$\varepsilon_{ion,\perp}$	4.98	4.98	4.41	4.08[a]
$\varepsilon_{ion,\parallel}$	5.76	5.76	5.17	4.99[a]
$\varepsilon_{0,\perp}$	10.27	8.21	7.64	7.78[a]
$\varepsilon_{0,\parallel}$	10.88	9.02	8.43	8.74[a]

[a]Reference [11]

Energy Change

By estimating the tolerance parameter, a picture of how close the calculated solutions are to the exact solutions are provided. The tolerance parameter was determined to be 10^{-6} eV by comparing the different results with the experimental values, shown in Table 3.6.

Table 3.6: Ionic contribution to the static dielectric constant.

Energy Change (eV)	$\varepsilon_{ion,\perp}$	$\varepsilon_{ion,\parallel}$
10^{-3}	4.31	5.17
10^{-4}	4.340	5.20
10^{-5}	4.40	5.16
10^{-6}	4.40	5.15
10^{-7}	4.40	5.15
Exp	4.08[a]	4.99[a]

[a]Reference [11]

3.4 Numerical Optimization

The convergence tests that have been performed contributes to achieving numerically converged results. In addition to the convergence tests, it is convenient to optimize the crystal structure of each material. This means that the positions of the atoms in the unit cell, the size and the shape of the unit cell are optimized in order to minimize the local energy. This is done by iterative algorithms that minimize the interatomic forces. The number of iterations are controlled by a tolerance parameter. The numerical optimization is called relaxation and was performed before proceeding with the the optical and electronic calculations.

The conclusion from the convergence tests in Sect. 3.2 was to proceed with an energy cutoff of 400 eV for the optical and electronic calculations. For the relaxation calculations, the cutoff energy should be increased by 50%. Therefore, the relaxation calculations were performed with an energy cutoff of 600 eV. The optimization for ε-Ga_2O_3 were performed with milder tolerance parameters than the other materials.

Chapter 4

Results and Discussion

The different results provided by the calculations of this work are presented and compared to experimental values of the same properties. The crystalline structures, the lattice parameters, the electronic band structure, the density of states (DOS), the dielectric functions, the absorption coefficients, the static dielectric constant and the high-frequency dielectric constant are the properties presented for the materials considered in this work. The theoretical calculations performed in this work are zero temperature approaches. The experiments that have provided the values for comparison have mostly not been performed at ground state conditions. As described in section 2.1.1 the occupancy of electrons in the conduction bands increase with increasing temperature. This affects the accuracy of the ground state calculations, compared to the experiments. However, this influence is expected to be small.

4.1 Crystal Structures

In this chapter the crystalline properties of the materials are presented and discussed. The space group information for each material is listed in Table 4.1, found in existing literature. The crystal structure of a material and its symmetry operations can be found from the space group symbol and its corresponding space group number. The Wyckoff position, describe the positions of the atoms in a material unit cell.

ε-Ga_2O_3, w-ZnO and α-SiO_2 are non-centrosymmetric, seen from the space groups listed in Table 4.1. The non-centrosymmetry give rise to special dielectric properties. The materials are piezoelectric. Hence, the material can be polarized with both an electrical field and mechanical stress.

Table 4.1: The crystal space group for each material with its number and Hermann Mauguin Symbol. The Wyckoff positions for the atoms in each material is also listed and the number indicate the number of inequivalent atoms present in the unit cell.

Material	Space Group		Wyckoff Position
	Nr.	Symbol	Cation / Anion
w-ZnO	186	$P6_3mc$[n]	2b / 2b[o]
α-SiO_2	154	$P3_221$[a]	3a / 6c[b]
a-TiO_2	141	$I4_1/amd$[e]	4a / 8e[f]
r-TiO2	136	$P4_2/nmm$[e]	2a / 4f[m]
a-SnO	129	P4/nmm[c]	2c / 2a[d]
r-SnO2	136	$P4_2/nmm$[k]	2a / 4f[l]
β-Ga_2O_3	12	C2/m[g]	4i / 4i[h]
ε-Ga_2O_3	33	$Pna2_1$[i]	4a / 4a[j]

[a]Reference [2] [b]Reference [40] [c]Reference [35] [d]Reference [44] [e]Reference [29] [f]Reference [39] [g]Reference [25] [h]Reference[41] [i]Reference [8] [j]Reference [42] [k]Reference [9] [l]Reference [45] [m]Reference [43] [o]Reference [46] [n]Reference [24]

The calculated lattice parameters and the corresponding experimental values are listed in Table 4.2. Only the monoclinic β-Ga_2O_3 and the orthorhombic ε-Ga_2O_3 have unlike lattice parameters a and b. For the remaining materials, $a = b$. The calculated values are in consistency $\pm$ 0.02 Å for the lattice parameter a, with an exception of α-SiO_2 which has a higher difference between computation and experimental values. For the lattice parameter c, the difference between the calculated and experimental values is also less than $\pm$0.02 Å for the last five materials listed in Table 4.2. a-SnO shows the largest deviation from the trend with a difference of $\pm$0.13 Å for the parameter c.

Table 4.2: Lattice parameters a, b and c in units of Å for all the materials. The calculated (Calc) values are compared with experimental (Exp) values.

	a		b		c	
	Calc	Exp	Calc	Exp	Calc	Exp
w-ZnO	3.25	3.25[f]	-	-	5.22	5.21[f]
α-SiO_2	4.97	4.913[a]	-	-	5.45	5.404[a]
a-TiO_2	3.79	3.7842[c]	-	-	9.60	9.5146[c]
r-TiO_2	4.57	4.5937[c]	-	-	2.95	2.9581[c]
a-SnO	3.79	3.81[b]	-	-	4.97	4.84[b]
r-SnO_2	4.74	4.74[e]	-	-	3.19	3.19[e]
β-Ga_2O_3	12.24	12.23[d]	3.04	3.037[d]	5.79	5.798[d]
ε-Ga_2O_3	5.03	5.046[g]	8.66	8.702[g]	9.27	9.283[g]

[a]Reference [3]
[b]Reference [35]
[c]Reference [29]
[d]Reference [25]
[e]Reference [11]
[f]Reference [12]
[g]Reference [18]

The crystal structures in this work have been relaxed with a $\boldsymbol{k}$ mesh of $4 \times 4 \times 4$. The relaxed structures are visualised using the software *Visualization of Electronic and STructural Analysis*, VESTA. These structures are used throughout this thesis.

The crystal structures of w-ZnO and α-SiO_2 are presented respectively in Fig. 4.1a and Fig. 4.1b. Both materials have got hexagonal lattices, but only w-ZnO belongs to the hexagonal crystal system. α-SiO_2 has a trigonal crystal structure with three silicon atoms and six oxygen atoms per primitive unit cell. w-ZnO has two zinc atoms and two oxygen atoms in its primitive cell.

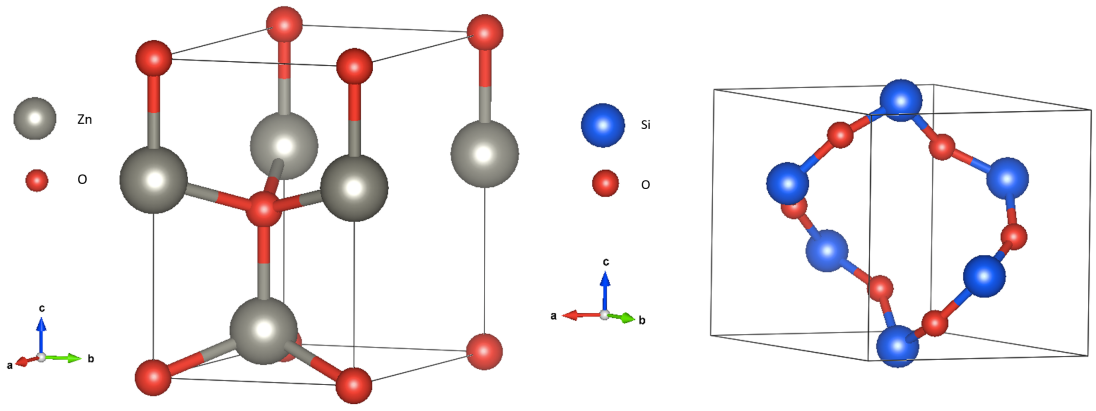

(a) (b)

Figure 4.1: The primitive cells of (a) w-ZnO and (b) α-SiO_2.

The space groups in Table 4.1 implies that a-SnO, r-SnO_2, a-TiO_2 and r-TiO_2 all crystallizes in tetragonal lattices. a-TiO_2 has a body centered tetragonal cell as illustrated in Fig. 4.2a, while the others have simple tetragonal cells. r-TiO_2 has two titanium atoms and four oxygen atoms in its primitive cell, which is illustrated in Fig. 4.2b.

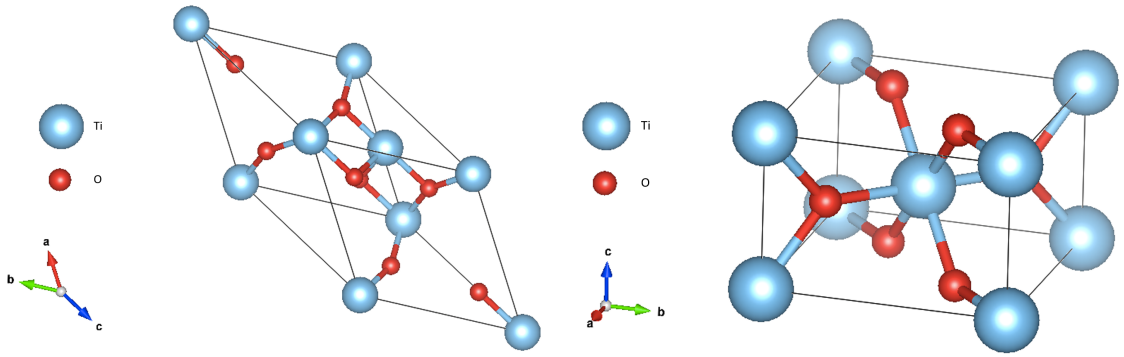

(a) (b)

Figure 4.2: The primitive cells of of (a) a-TiO_2 and (b) r-TiO_2.

a-SnO crystallizes in a simple tetragonal structure with two tin atoms and two oxygen atoms per primitive unit cell and is presented in Fig. 4.3a. The simple tetragonal structure of r-SnO_2 is presented in Fig. 4.3b and consists of two tin oxides and four oxygen atoms.

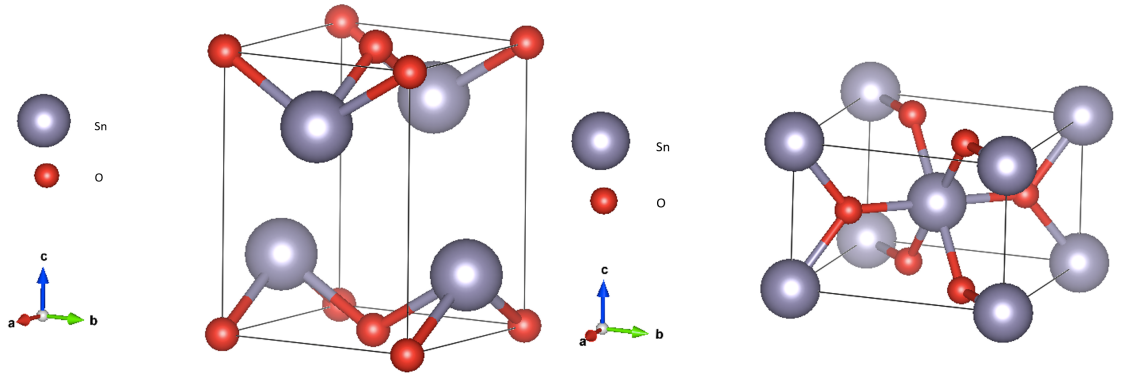

(a) (b)

Figure 4.3: The primitive cells of of (a) a-SnO and (b) r-SnO_2.

β-Ga_2O_3 crystallizes in a C-centered monoclinic structure, visualised in Fig. 4.4a. ε-Ga_2O_3 crystallizes in an orthorhombic structure, which is shown in Fig. 4.4b. The calculated β-angle for β-Ga_2O_3 is 103.76°, which is in good consistency with the experimental value of 103.7° [25].

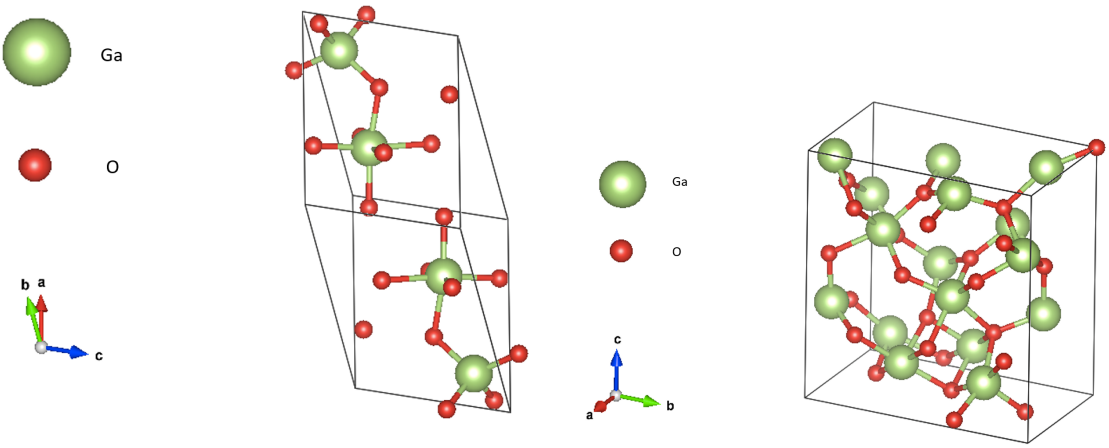

(a) (b)

Figure 4.4: The primitive cells of of (a) β-Ga_2O_3 and (b) ε-Ga_2O_3.

4.2 Electronic Properties

In this section the calculated bandgap values and band structures for the different materials are presented. Each Brillouin zone represented in this section is constructed in accordance to the path recommended for the specific crystal lattice [31]. The electronic band structure for a material is calculated along the path corresponding to the materials Brillouin zone.

The estimation of bandgap energies for semiconductors using the Kohn-Sham approach in DFT is a known challenge. Hybrid functional calculations are reported to yield a better approach to the experimental values, compared to GGA calculations (including PBE functional). However, the calculated bandgap values in this work, presented in Table 4.3, vary for each material whether the resulting bandgap is overestimated or underestimated compared to the experimental values. For w-ZnO, r-SnO_2 and β-Ga_2O_3, the values are underestimated, while for a-SnO, r-TiO_2 and a-TiO_2 they are overestimated. As illustrated in Table 3.2 in Sect. 3.1, a trend exist where the bandgap value increases with the increase of the fraction of Hartree-Fock energy in the exchange-correlation energy. Hence, the materials with underestimated values presented in Table 4.3 might get better bandgap calculations with a higher fraction of Hartree-Fock energy, while the opposite might show better results for the materials with overestimated values.

Table 4.3: Bandgap energy in unit eV for each material. The calculated (Calc) values are compared with experimental (Exp) values. The values describe the direct transition at the Γ-point, unless it is an indirect transition, noted with (i).

	Calc	Exp
w-ZnO	3.03	3.4[a]
a-SiO_2	8.51, 8.15 (i)	9.1[b]
a-TiO_2	4.13, 3.71 (i)	3.20[c]
r-TiO_2	3.70	3.0[c]
a-SnO	2.83, 0.73 (i)	2.8[a], 0.7(i)[a]
r-SnO_2	3.37	3.6[a]
b-Ga_2O_3	4.64	4.85 ± 0.1 (i) [d]
e-Ga_2O_3	4.75	-

[a]Reference [11]
[b]Reference [3]
[c]Reference [29]
[d]Reference [36]

A path through the high-symmetry points in the Brillouin zone belonging to the hexagonal lattice is illustrated in Fig. 4.5a. The band structure for w-ZnO was calculated for this path, as w-ZnO has a hexagonal lattice. The calculation for the whole path Γ-M-K-Γ-A-L-H-A is performed with a PBE functional to provide a complete presentation of the shape of the band structure. From the PBE band structure, Fig. 4.5b, it is obvious that w-ZnO exhibits a direct bandgap at the Γ-point, because both the valence band maximum (VBM) and the conduction band minimum (CBM) are located there.

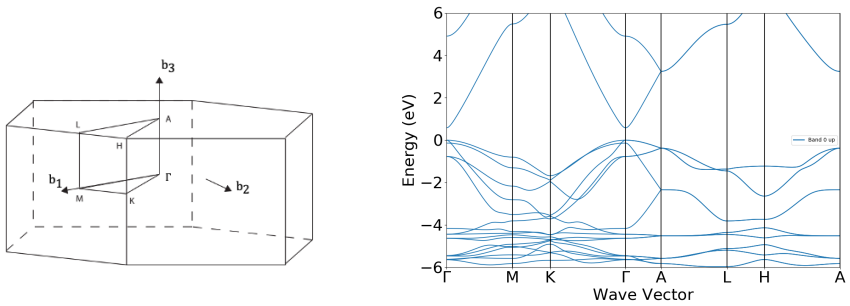

(a) (b)

Figure 4.5: (a) Brillouin zone of a hexagonal lattice with path: Γ-M-K-Γ-A-L-H-A and (b) the electronic band structure of w-ZnO along this path.

A hybrid functional calculation for the most interesting high-symmetry points was performed in order to take a closer look at the bands. For w-ZnO this was conducted for the path K-Γ-A, resulting in Fig. 4.6. A very clear difference between the PBE calculated electronic band structure in Fig. 4.5b and the hybrid functional calculated electronic band structure in Fig. 4.6 is the bandgap between the VBM and the CBM. These figures really illustrate the significance of the exchange-correlation energy. In all the electronic band structure calculations, the energy equal to zero refers to the energy of the VBM for each respective material. A close study of Fig. 4.6 in the wave vector region K−Γ in the energy range -2 to -4 reveal an error due to bandcrossing in DFT. Figure 4.6 also shows the projected density of states (DOS) within the same energy range as for the band structure. It reveals that it is the O-2p bands that contribute the most to the VBM and the Zn-3d to the CBM.

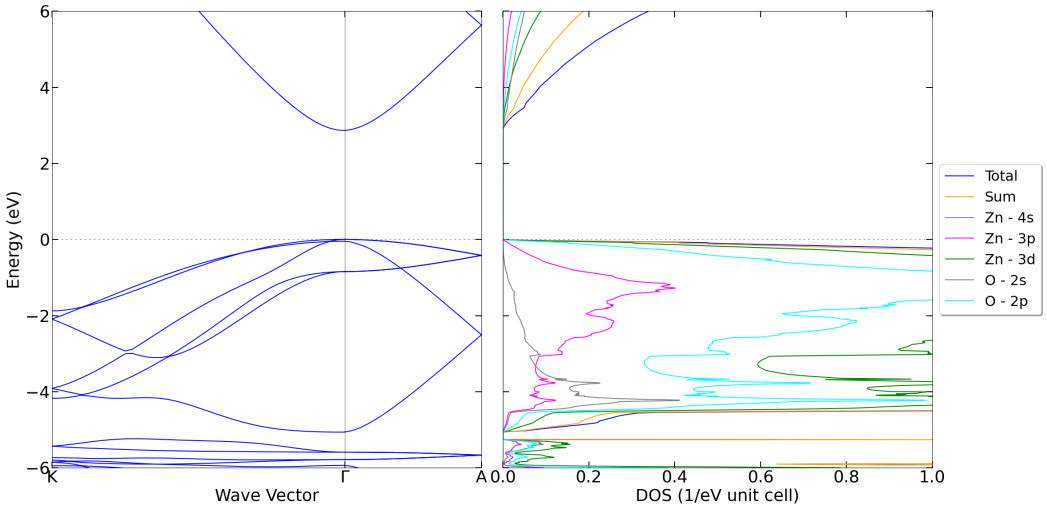

Figure 4.6: Electronic band structure of ZnO for the path K-Γ-A and the corresponding density of states for the unit cell within the energy range -6 to 6 eV.

The calculations described for w-ZnO were performed for all the materials, with respect to their Brillouin zone. The figures of band structures containing more than three high symmetry points are results of PBE calculations, while the figures of band structures with only three high symmetry points and DOS are results from hybrid functional calculations. Both the PBE and the hybrid functional calculations of the band structure were performed with a $\boldsymbol{k}$-mesh of $4 \times 4 \times 4$. The DOS calculations on the other hand were calculated with a greater $\boldsymbol{k}$ mesh, $10 \times 10 \times 10$. In each DOS calculation, the total DOS is plotted, and assigned "Total" in addition to the "Sum", referring to the calculated sum of the atom projected DOS.

Another material with a hexagonal cell is α-SiO_2. Unlike w-ZnO, this material does not exhibit a direct bandgap. Figure 4.7 and Fig. 4.8 reveal that the VBM is located at the K point and the

CBM is located at the Γ-point. The difference between the hybrid functional calculated direct and the indirect gaps is only 0.36 eV, with the direct gap referring to a Γ-Γ transition.

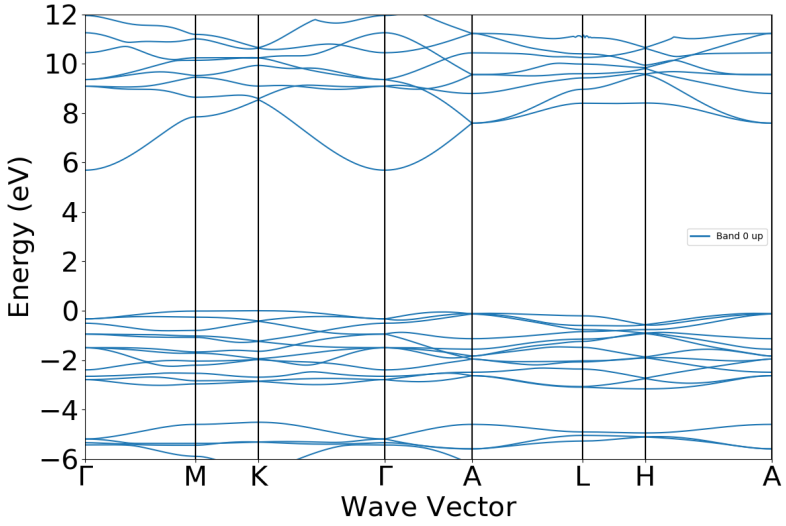

Figure 4.7: Electronic band structure of α-SiO_2 for the path: Γ-M-K-Γ-A-L-H-A.

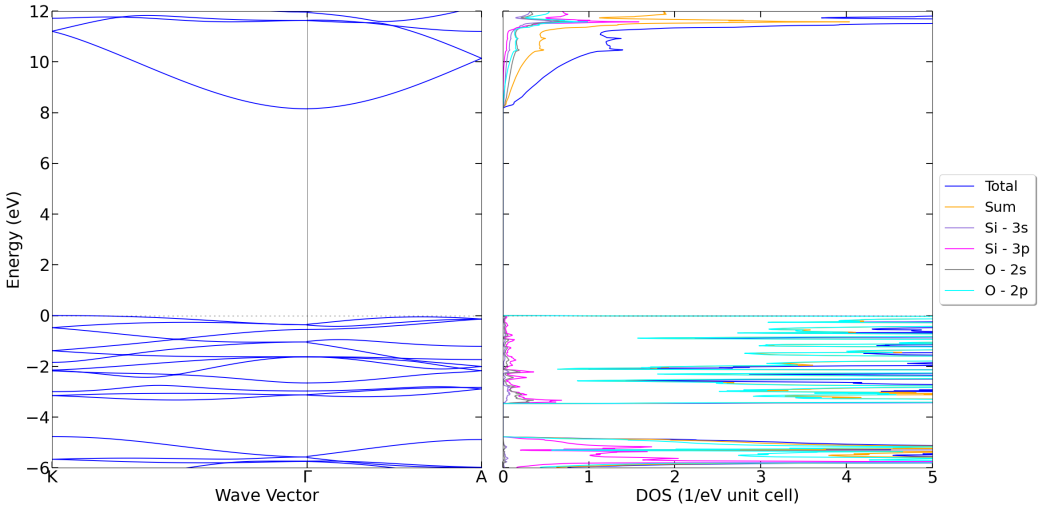

Figure 4.8: The electronic band structure of α-SiO_2 with a shorter path: K-Γ-A and the corresponding DOS for the unit cell within the energy range -6 to 12 eV.

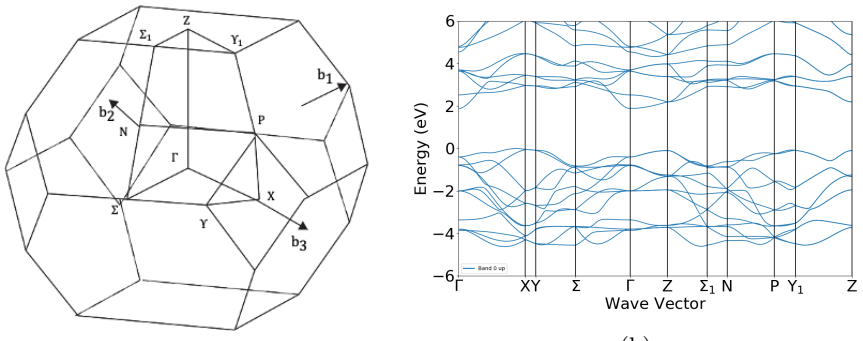

(a) (b)

Figure 4.9: (a) Brillouin zone of a body centered tetragonal lattice with path: Γ-X-Υ-Σ-Γ-Z-Σ_1-N-P-Υ_1-Z and (b) the band structure of a-TiO2 along this path.

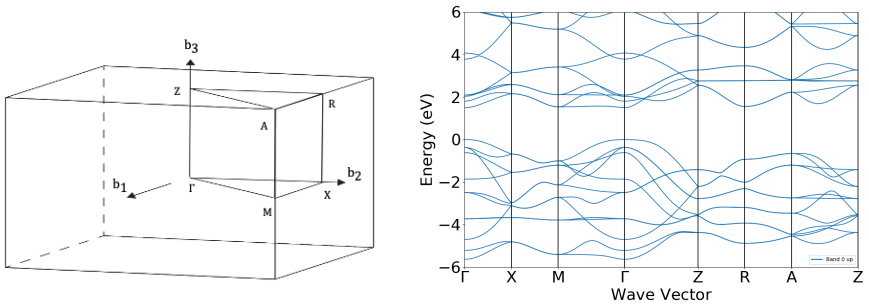

(a) (b)

Figure 4.10: (a) Brillouin zone of a simple tetragonal lattice with path: Γ-X-M-Γ-Z-R-A-Z and (b) the band structure of r-TiO2 along this path.

The unit cell of r-TiO_2 is simple tetragonal, while a-TiO_2 has a body-centered tetragonal cell. The corresponding Brillouin zones are represented in Fig. 4.10a and Fig. 4.9a. Both polymorphs have their CBM located in the Γ-point, as seen in Fig. 4.9b and 4.10b. r-TiO_2 also has the VBM located at this point. The VBM of a-SiO_2 is located at the Z-point in the Brillouin zone of the body-centered tetragonal lattice. Naturally, for both materials, it is the same orbitals that contribute the most to the bands near their Fermi level. It is the Ti $3d$ orbitals and the O $2p$ orbitals, as the DOS in the figures 4.11 and 4.12 reveals.

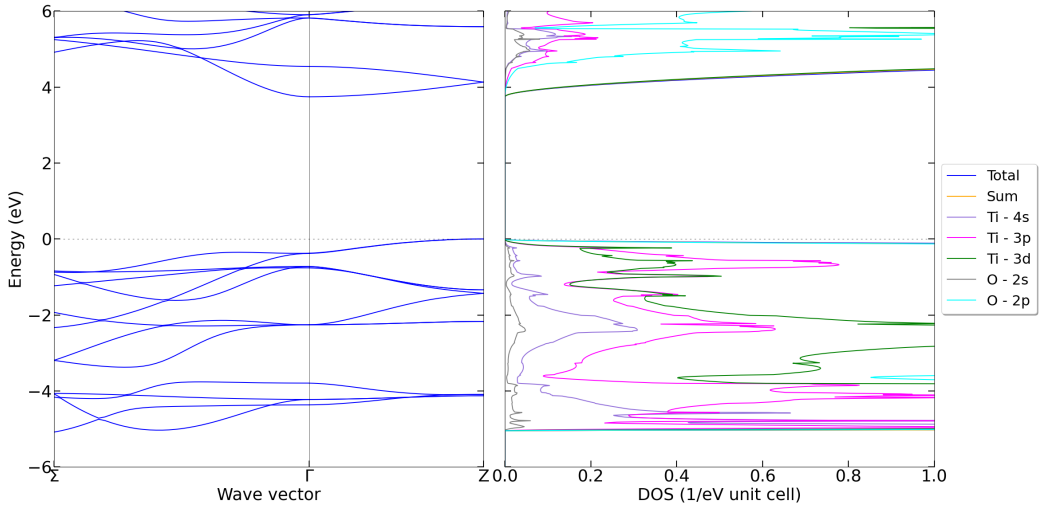

Figure 4.11: Electronic band structure for the path Σ- Γ-Z for a-TiO_2 and the corresponding density of states for the unit cell within the energy range -6 to 6 eV.

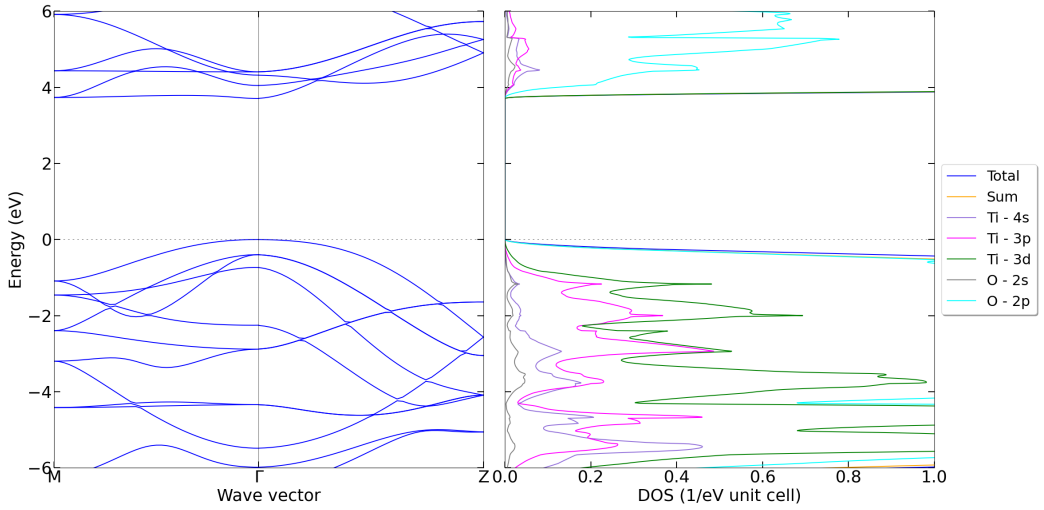

Figure 4.12: Electronic band structure for the path M-Γ-Z for r-TiO_2 and the corresponding density of states for the unit cell within the energy range -6 to 6 eV.

A similar comparison can be made between a-SnO and r-SnO_2 as for between a-TiO_2 and r-TiO_2. From an inspection of Fig. 4.13a and Fig. 4.13b it is obvious that the anatase phases exhibits an indirect bandgap, while the rutile ones have a direct gap at the Γ-point. a-SnO has its VBM located at the Γ-point and the CBM located at the M-point. Both a-SnO and r-SnO_2 have the same unit cell lattice as r-TiO_2, a simple tetragonal lattice, illustrated in Fig. 4.10a. The band structures are calculated in the path corresponding to this Brillouin zone. The indirect bandgap of a-SnO is, as the data in Table 4.3 shows, very narrow, and the orbitals contributing mostly to is the Sn $5p$ orbitals. There is in general a greater DOS for r-SnO_2 than for a-SnO, as seen by comparing the figures 4.14 and 4.15, which is not suprising due to the difference in atoms in their unit cell.

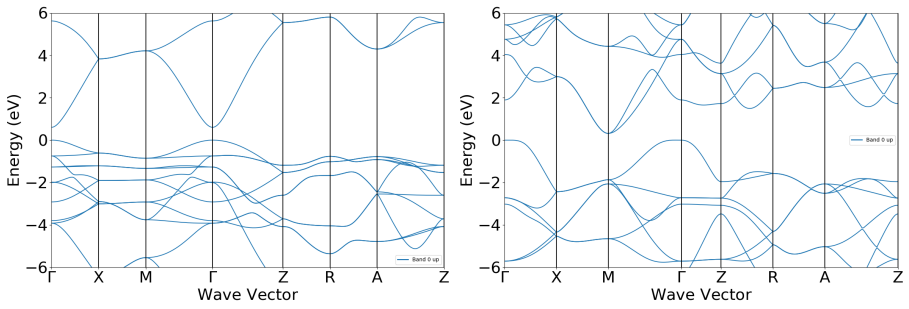

Figure 4.13: (a) The electronic band structure for r-SnO_2 and (b) a-SnO along the path Γ-X-M-Γ-Z-R-A-Z.

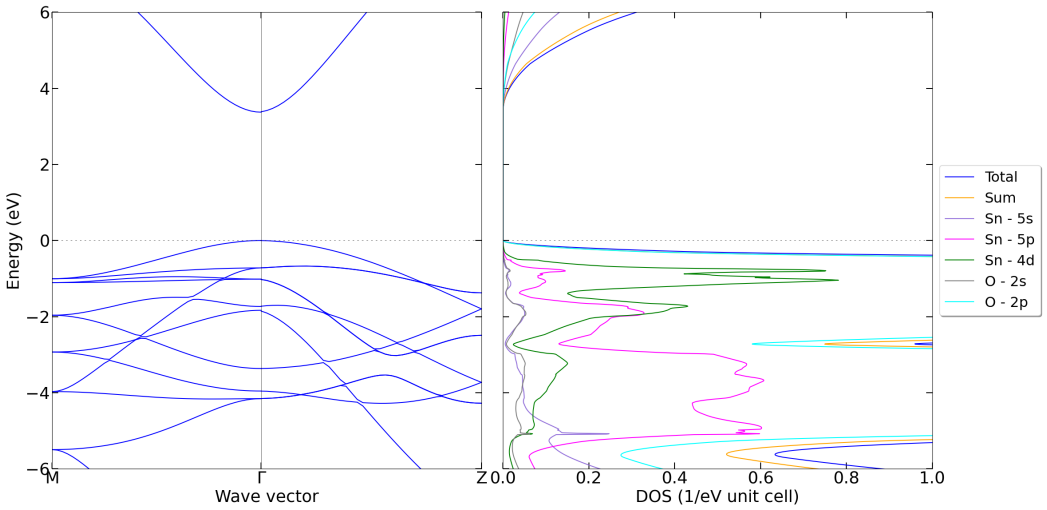

Figure 4.14: Electronic band structure for the path M-Γ-Z for r-SnO_2 and the corresponding density of states for the unit cell within the energy range -6 to 6 eV.

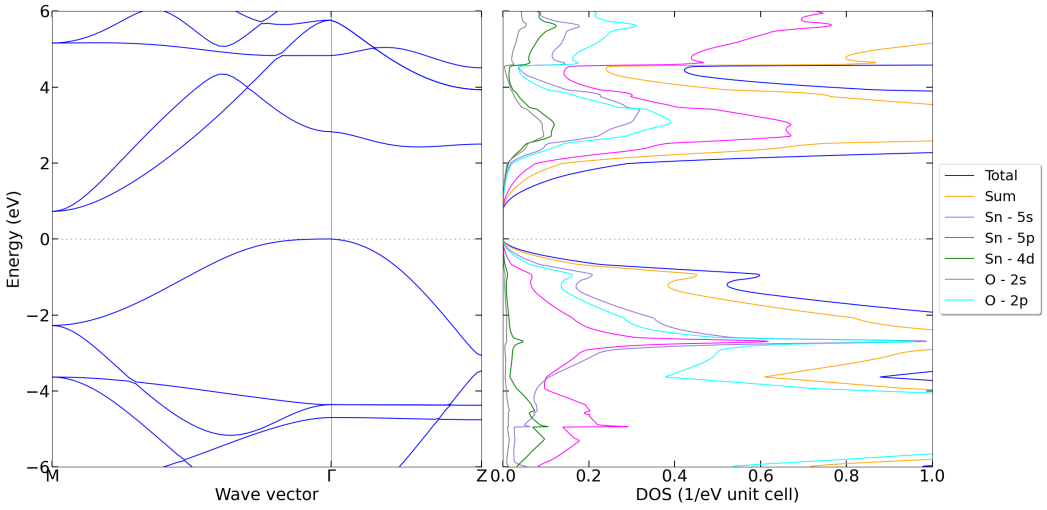

Figure 4.15: Electronic band structure for the path M-Γ-Z for a-SnO and the corresponding density of states for the unit cell within the energy range -6 to 6 eV.

The Brillouin zones for β-Ga_2O_3 and ε-Ga_2O_3 are illustrated in Fig. 4.16a and Fig. 4.17a respectively. Their band structures are presented in Fig. 4.16b and Fig. 4.17b. By comparing Fig. 4.18 with Fig. **??** it is clear that ε-Ga_2O_3 has far more bands at the Γ point compared to β-Ga_2O_3. This is as expected since ε-Ga_2O_3 has 40 atoms in its unit cell, contributing to the energy bands, while β-Ga_2O_3 only has 10 atoms in its unit cell.

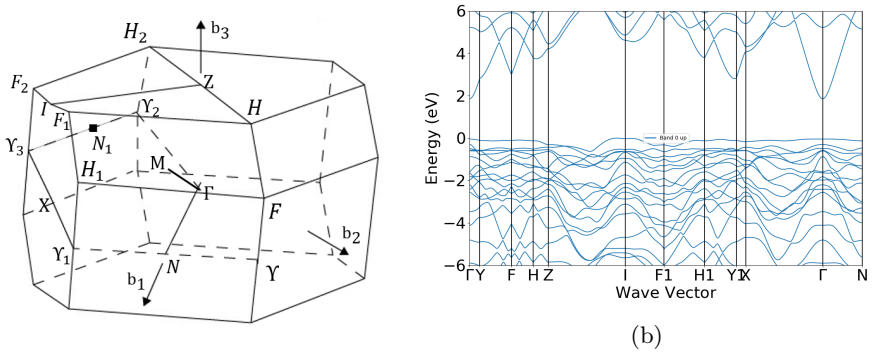

(a) (b)

Figure 4.16: (a) Brillouin zone of an orthorhombic lattice with path: Γ-ϒ-F-H-Z-I-F_1-H_1-$ϒ_1$-X-Γ-N and (b) the band structure of β-Ga_2O_3 along this path.

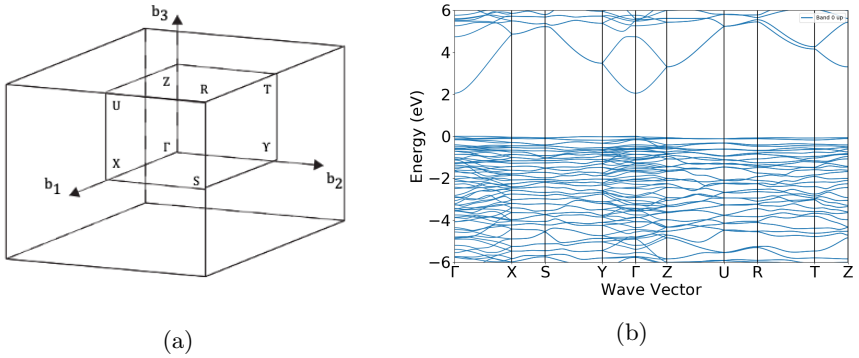

(a) (b)

Figure 4.17: (a) Brillouin zone of an orthorhombic lattice with path: Γ-X-S-ϒ-Γ-Z-U-R-T-Z and (b) the band structure of ε-Ga_2O_3 along this path.

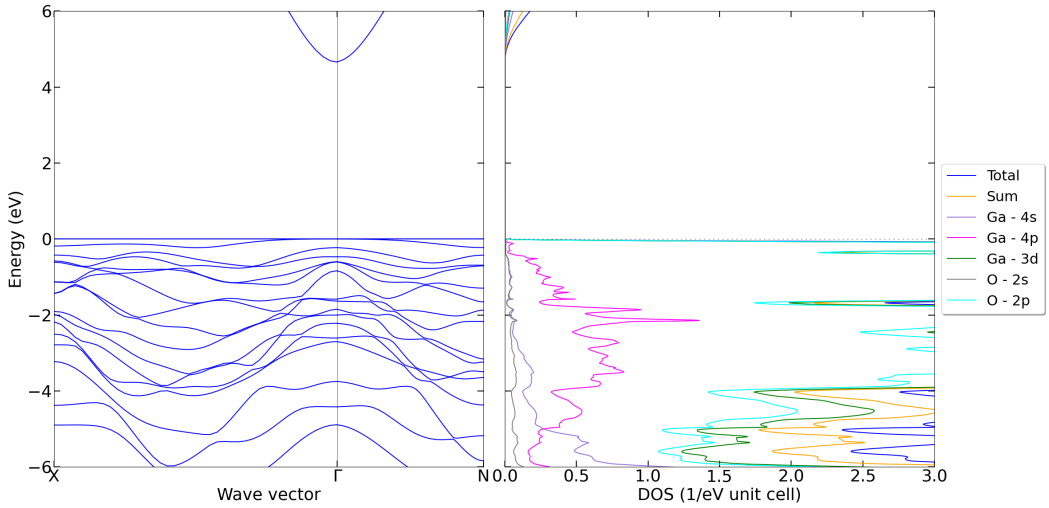

Figure 4.18: Electronic band structure for the path X-Γ-N for β-Ga_2O_3 and the corresponding density of states for the unit cell within the energy range -6 to 6 eV.

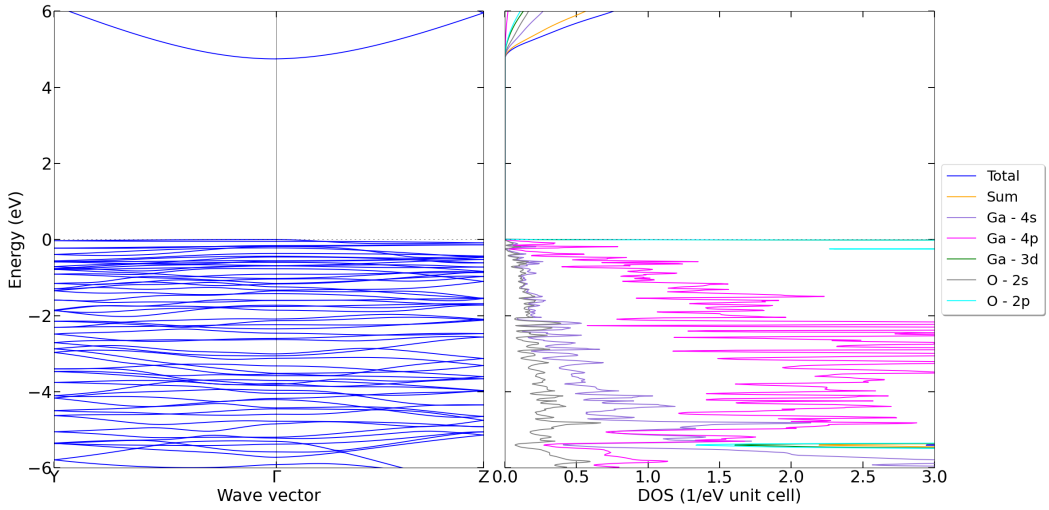

Figure 4.19: Electronic band structure for the path ϒ-Γ-Z for ε-Ga_2O_3 and the corresponding density of states for the unit cell within the energy range -6 to 6 eV.

For all the materials there is a difference in the total DOS and the sum of the atom-projected DOS. The atomic projections do not overlap, in order for each projected DOS to not contain contribution from other atoms. A consequence of this approach is that the interstitial states are lost. The difference in the total DOS and the sum of the atom-projected DOS illustrates the density of states which are delocalized. This difference increases as the energy increases.

4.3 Dielectric Properties

Herein the calculated high frequency dielectric constants and the static dielectric constants are presented for all the materials and compared with experimental values. Also, the dielectric functions are illustrated in figures for each material. In addition the high frequency functions and absorption coefficients are visualised in figures all together in order to achieve a better comparison of the materials.

The calculated high-frequency dielectric constants and static dielectric constants are presented in Table 4.4, along with the corresponding experimental values. However, some of the experimental values have not been accounted for. It seems to be a trend in underestimating the constants. All though, the static constants of r-TiO_2 are extreme examples of the opposite. A deviation of +137.45 and +171.36 is seen respectively for the transverse and the longitudinal component of the static dielectric constant compared to the experimental values. This indicates that the crystal structure of r-TiO_2 is highly sensitive to relaxation. These calculated values are very much overestimated. The experimental values of the high-frequency dielectric constants have to be measured at energy levels where the ionic contribution is no longer significant. This could result in measured values for the high-frequency dielectric constants that are larger than the real high-frequency dielectric constants.

The dielectric constants calculated for w-ZnO are in alignment with the experimental values with an error rate of approximately 13 % for the high frequency constants and less than 3.5 % for the static constants. w-ZnO has the smallest error rate compared to the experimental values among the materials in this project. Therefore, it is reasonable to think that the convergence tests might have contributed to better results if the reference material had been another than w-ZnO. The dielectric constants are sensitive to relaxation, which was illustrated by the data listed in Table 3.5 in Sect. 4.3. A PBE-relaxed w-ZnO structure resulted in the transverse and longitudinal high-frequency constants of 5.29 and 5.12, which is an overestimation of +1.59 and +1.86 compared to the experimental values. An overestimation compared to experimental values are also seen for the static constants calculated with a PBE-relaxed structure in Table 3.5. It would be reasonable to expect that stricter convergence criterion for relaxation and self-consistency would result in better approximations of the dielectric constants. However, this again comes at the expense of computational resources. Never the less, it was clear from Table 3.5 in Sect. 4.3 that when compared to experimental values, the HSE calculations provided much better results than the PBE calculations. PBE also provides poor bandgap values and from the Moss relation it is known that the dielectric constants for a material decrease with the increase of bandgap value.

Table 4.4: The high-frequency dielectric constants, $\varepsilon_{\infty,\perp}$ and $\varepsilon_{\infty,\parallel}$, and the static dielectric constants, $\varepsilon_{0,\perp}$ and $\varepsilon_{0,\parallel}$. The experimental (Exp) and calculated (Calc) values are listed.

Material	$\varepsilon_{\infty,\perp}$		$\varepsilon_{\infty,\parallel}$		$\varepsilon_{0,\perp}$		$\varepsilon_{0,\parallel}$	
	Calc	Exp	Calc	Exp	Calc	Exp	Calc	Exp
w-ZnO	3.23	3.70[a]	3.26	3.75[a]	7.64	7.78[a]	8.44	8.74[a]
α-SiO_2	2.18	-	2.19	-	4.31	4.6	4.51	4.51
a-TiO_2	4.84	5.8[b]	4.79	5.4[b]	47.03	45[b]	24.15	23[b]
r-TiO_2	4.97	6.8[b]	5.73	8.4[b]	223.45	86[b]	241.36	170[b]
r-SnO_2	3.26	3.8[b]	3.54	4.2[b]	12.17	14[b]	8.28	9.6[b]
a-SnO	6.06	7.8[c]	5.28	7.25[c]	16.86	-	10.73	-

[a]Reference [11]
[b]Reference [9]
[c]Reference [35]
[d]Reference [36]
[e]Reference [6]

β-Ga_2O_3 and ε-Ga_2O_3 exhibit anisotropy in all directions, hence, the dielectric constants for

these are presented in Table 4.5.

Table 4.5: The high-frequency dielectric constants $\varepsilon_{\infty,i}$ for the tensor components $i = xx, yy, zz$ and the static dielectric constants $\varepsilon_{0,i}$ for $i = xx, yy, zz$ for β-Ga_2O_3. The experimental (Exp) and calculated (Calc) values are listed.

	β-Ga_2O_3		ε-Ga_2O_3	
	Calc	Exp	Calc	Exp
$\varepsilon_{\infty,xx}$	3.10	-	2.25	-
$\varepsilon_{\infty,yy}$	3.19	-	2.15	-
$\varepsilon_{\infty,zz}$	3.15	-	2.15	-
$\varepsilon_{0,xx}$	10.11	9.9-10.2[a]	14.38	-
$\varepsilon_{0,yy}$	9.37	-	13.25	-
$\varepsilon_{0,zz}$	13.07	13.9[a]	17.46	-

[a]Reference [36]

The dielectric functions are presented in the figures 4.20 to 4.26 for w-ZnO, α-SiO_2, a-TiO_2, r-TiO_2, a-SnO, r-SnO_2, β-Ga_2O_3, and ε-Ga_2O_3 respectively. The figures are separated in a real part (a) and an imaginary part (b) of the dielectric function. The longitudinal and the transverse frequency dependent functions without local field effects are visualized as $\varepsilon \perp$ and $\varepsilon \parallel$. The local field effects are added to the figures and denoted as $\varepsilon_i, \perp$ and $\varepsilon_i, \parallel$. The ionic contribution is only significant at low energy levels. In order to study the ionic contribution better, the figures are zoomed in at the energy range 0 to 0.2 eV. The direct bandgap and indirect bandgap values are also outlined in the figures and denoted as E_G and E_{Gi} respectively, in order to study the electronic response in light of the bandgap.

α-SiO_2 shows ionic polarization at several energy levels, seen by the many peaks in the energy range 0 to 0.1 eV in Fig. 4.21b, meaning that the ions in α-SiO_2 are sensitive to an applied field at these energy levels. While w-ZnO only show a wider peak at approximately 0.05 eV, in Fig. 4.20b. With only one peak it is reasonable to conclude that there are stronger intermolecular forces in the w-ZnO crystal than in the α-SiO_2 crystal. Considering the imaginary part of the dielectric function for α-SiO_2 shown in Fig. 4.21b, both the direct and indirect bandgap are located below electronic polarization. This indicates that a transition from VBM to CBM is forbidden.

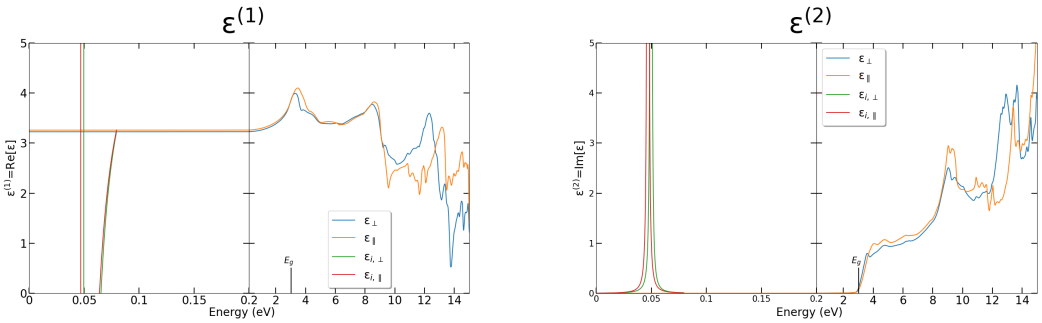

(a) (b)

Figure 4.20: (a) The real part and (b) the imaginary part of the dielectric function for w-ZnO. The figures are separated in two parts with different energy steps. This has been done to give a better presentation of the ionic contribution to the dielectric functions in the energy range of 0 to 0.2 eV.

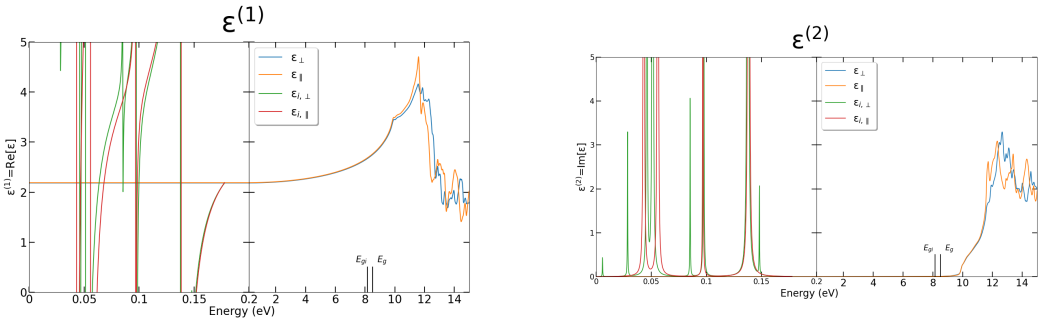

(a) (b)

Figure 4.21: (a) The real part and (b) the imaginary part of the dielectric function for α-SiO_2. The figures are separated in two parts with different energy steps. This has been done to give a better presentation of the ionic contribution to the dielectric functions in the energy range of 0 to 0.2 eV.

a-TiO_2 and r-TiO_2 have quite similar dielectric functions. For a-TiO_2 the anisotropy is seen near the CBM for the imaginary part of the dielectric function in Fig. 4.22b. Only the transverse component of the high frequency dielectric function show polarization at the direct bandgap energy level. The same anisotropy is not seen for r-TiO_2 in Fig. 4.23b. However, r-TiO_2 does not have corresponding location for the polarization and the direct bandgap value, indicating that a transition from VBM to CBM is forbidden. r-TiO_2 shows a strong ionic polarization in the range of 0 to approximately 0.04 eV, hence the material might absorb infrared radiation in this energy region.

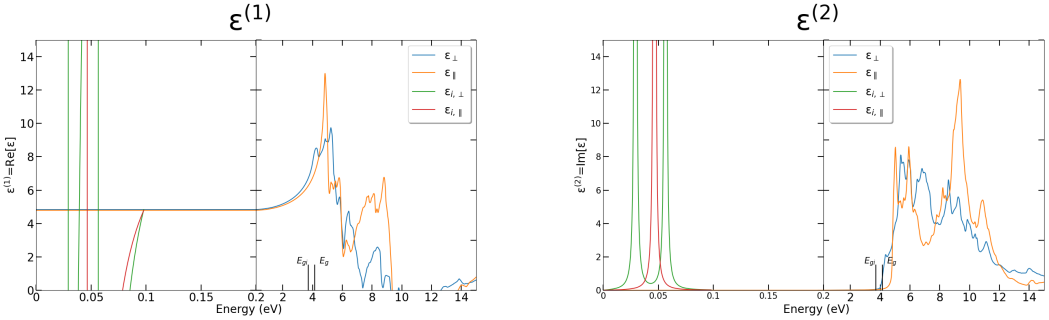

(a) (b)

Figure 4.22: (a) The real part and (b) the imaginary part of the dielectric function for a-TiO_2. The figures are separated in two parts with different energy steps. This has been done to give a better presentation of the ionic contribution to the dielectric functions in the energy range of 0 to 0.2 eV.

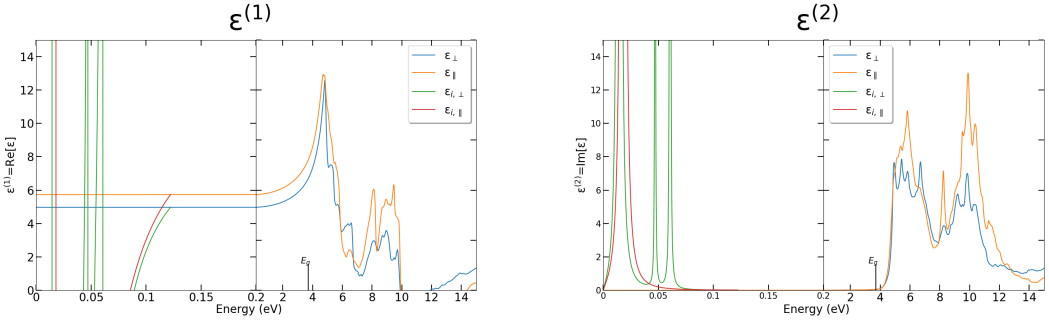

(a) (b)

Figure 4.23: (a) The real part and (b) the imaginary part of the dielectric function for r-TiO_2. The figures are separated in two parts with different energy steps. This has been done to give a better presentation of the ionic contribution to the dielectric functions in the energy range of 0 to 0.2 eV.

The dielectric functions for a-SnO and r-SnO_2 are presented in Fig. 4.24 and Fig. 4.25 respectively. r-SnO_2 has three distinct peaks showing the ionic polarization at these energy levels, while a-SnO only has two. a-SnO has a small indirect gap at 0.72 eV, listed in Table 4.3 in Sect. 4.2. By studying the imaginary part of the dielectric function in Fig. 4.24b it is clear that this value does not correspond to the location of the electronic response. The direct bangap however, is more consistent with the polarization. As for r-TiO_2 and α-SiO_2, a small deviation between the polarization and the estimated bandgap value exist for r-SnO_2, and is illustrated in Fig. 4.25b. The magnitude of electronic polarizability is greater for a-SnO than for r-SnO_2, which leads to the conclusion that the intermolecular forces are weaker within the a-SnO crystal than within the r-SnO_2 crystal.

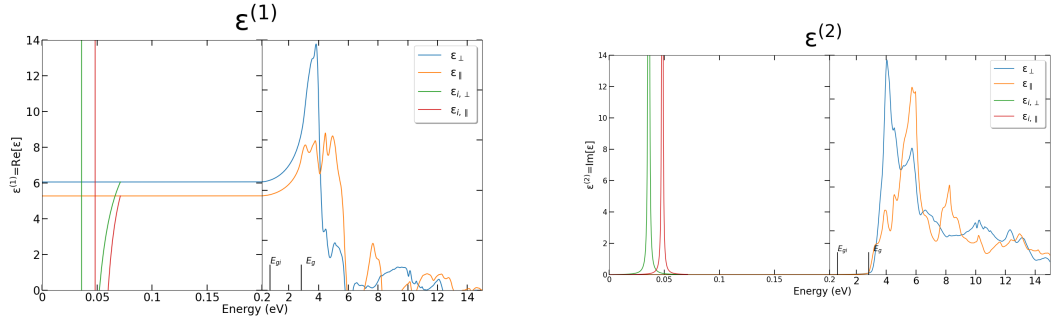

(a) (b)

Figure 4.24: (a) The real part and (b) the imaginary part of the dielectric function for a-SnO. The figures are separated in two parts with different energy steps. This has been done to give a better presentation of the ionic contribution to the dielectric functions in the energy range of 0 to 0.2 eV.

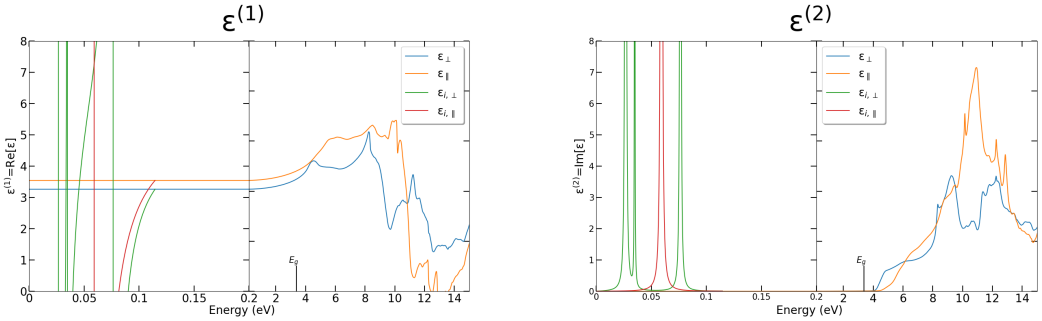

(a) (b)

Figure 4.25: (a) The real part and (b) the imaginary part of the dielectric function for r-SnO_2. The figures are separated in two parts with different energy steps. This has been done to give a better presentation of the ionic contribution to the dielectric functions in the energy range of 0 to 0.2 eV.

β-Ga_2O_3 shows a strong ionic polarization, illustrated by all the peaks in the energy region 0 to 0.2 eV in Fig. 4.26. It is the *yy*-component that shows the greatest magnitude in electronic polarization, seen by the peak in Fig. 4.26b at approximately 12 eV. However, it is the *xx*- and *zz* components that contribute to absorption closest to the CBM at approximately 5 eV. The ionic polarization seen in Fig. 4.27 for ε-Ga_2O_3 is even stronger than observed for β-Ga_2O_3. However, as described in Sect. 3.4, the relaxation for ε-Ga_2O_3 was performed with milder tolerance parameters compared to the other materials. This might contribute to a stronger polarization for ε-Ga_2O_3 as the ionic contribution is highly dependent on the relaxation of the structures.

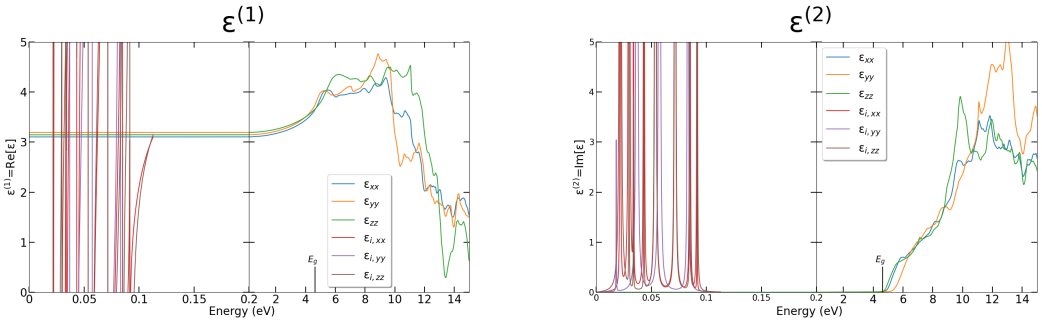

(a) (b)

Figure 4.26: (a) The real part and (b) the imaginary part of the dielectric function for β-Ga_2O_3. The figures are separated in two parts with different energy steps. This has been done to give a better presentation of the ionic contribution to the dielectric functions in the energy range of 0 to 0.2 eV.

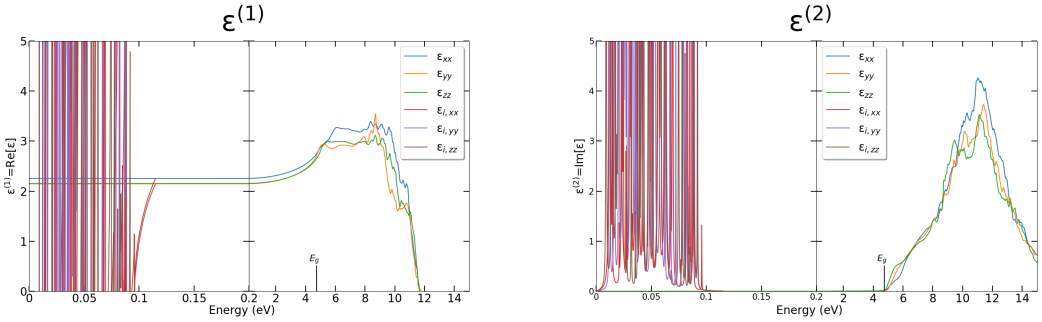

(a) (b)

Figure 4.27: (a) The real part and (b) the imaginary part of the dielectric function for ε-Ga_2O_3. The figures are separated in two parts with different energy steps. This has been done to give a better presentation of the ionic contribution to the dielectric functions in the energy range of 0 to 0.2 eV.

The Moss relations states that the high frequency dielectric constants are inversely proportional to the a materials bandgap. This trend is seen within the same material. However, it would be interesting to evaluate if this trend also applies when comparing different materials. Hence, the high-frequency dielectric constants with respect to the bandgap energies for each material is presented in Fig. 4.28. The figure reveals that there is no clear trend to observe. Never the less, it comfirms the Moss relation. By comparing a-SnO with r-SnO_2 , r-TiO_2 with a-TiO_2 and β-Ga_2O_3 with ε-Ga_2O_3 it is obvious that the phase with the lowest bandgap energy also has the highest high-frequency dielectric constant.

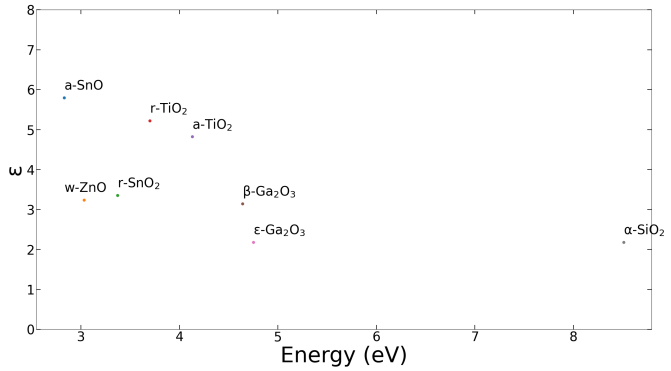

Figure 4.28: The geometric average of high-frequency dielectric constant, $\varepsilon_\infty = (\varepsilon_{\infty,xx} + \varepsilon_{\infty,yy} + \varepsilon_{\infty.zz})/3$ for a material with respect to its bandagap energy.

a-SnO, r-TiO_2, and a-TiO_2 have a similar trend in their response to an electromagnetic field. Their dielectric functions are presented in Fig. 4.29 and Fig. 4.30 along with the other materials considered in this project. These three materials show the strongest responses in the range 0 to 6 eV. This might not be too surprising since they have approximately the same lattice arrangement. a-SnO has its response peak at approximately 1 eV lower in energy than r-TiO_2 and a-TiO_2, which have their peaks located at the same energy. r-TiO_2 shows a stronger response than a-TiO_2, and can be seen by the height of the peaks. For the TiO_2-polymorphs it is the rutile phase that exhibits the strongest response, while for the tin oxides it is the anatase phase. However, it is important to keep in mind that a-SnO and r-SnO_2 have different ratios of elements in their respective unit cells. β-Ga_2O_3 and ε-Ga_2O_3 also show a similar trend to one another, but β-Ga_2O_3 show the strongest response among these two oxides. Due to its very large bandgap, α-SiO_2 shows a peak in dielectric response at approximately 11.5 eV. At lower energy levels than this, α-SiO_2 shows the weakest response among all the materials. This result was as anticipated since it is an insulator and not a semiconductor like the rest of the materials. The electrons in α-SiO_2 are more localized than in the semiconductors. w-ZnO also shows an overall weak response compared to the other materials. However, as most of the materials have a varying response, w-ZnO keeps it more or less steady, with a response at approximately $\varepsilon^{(1)} = 3$ at 0 eV and $\varepsilon^{(1)} = 2$ at 15 eV. The dielectric functions in Fig. 4.29 and Fig. 4.30 are calculated excluding local field effects. These field effects are instead shown for each individual material in the dielectric function figures 4.20 to 4.26.

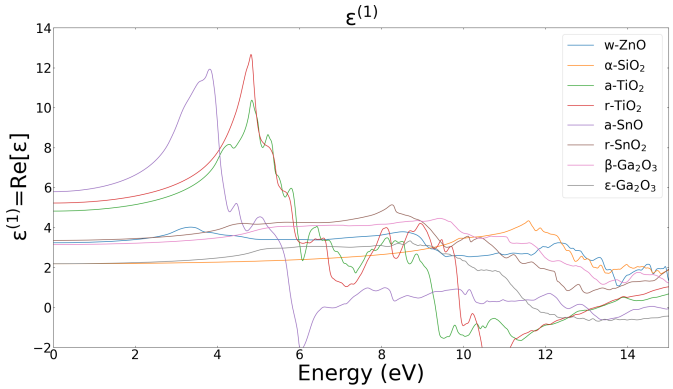

Figure 4.29: The geometric average of real part of the dielectric function, $\varepsilon^1 = (\varepsilon^1_{xx} + \varepsilon^1_{yy} + \varepsilon^1_{zz})/3$, for the respective materials considered in this work.

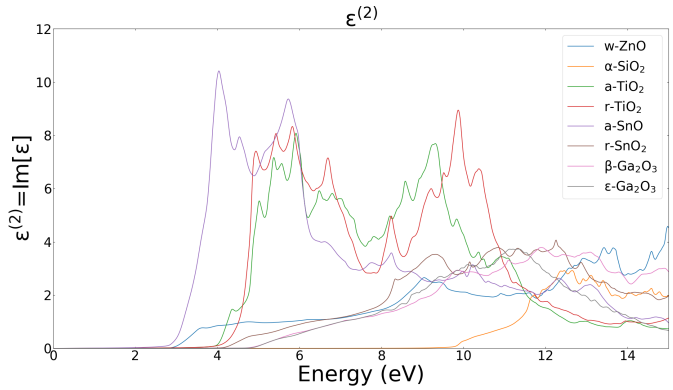

Figure 4.30: The geometric average of imaginary part of the dielectric function, $\varepsilon^1 = (\varepsilon^1_{xx} + \varepsilon^1_{yy} + \varepsilon^1_{zz})/3$, for the respective materials considered in this work.

The absorption coefficient for all the materials are presented in Fig. 4.31. These calculations are dependent on the dielectric functions, hence, these calculations do not include local field effects either. Materials with a significant amount of crystal vibrations, phonons, for example ε-Ga_2O_3, β-Ga_2O_3 and α-SiO_2, will absorb infrared radiation in the energy region 0 to 0.1 eV. The region of visible light extends up to 3.26 eV. By evaluating the absorption coefficients in Fig. 4.31 in the energy region around 3.26 eV, it is clear that only a-SnO and w-ZnO might absorb visible light.

However, this is not much. Hence, all the materials are expected to be transparent, which is due to their large bandgap energies. All the materials are expected to show absorbance of ultraviolet (UV) radiation, for energies higher than 3.26 eV.

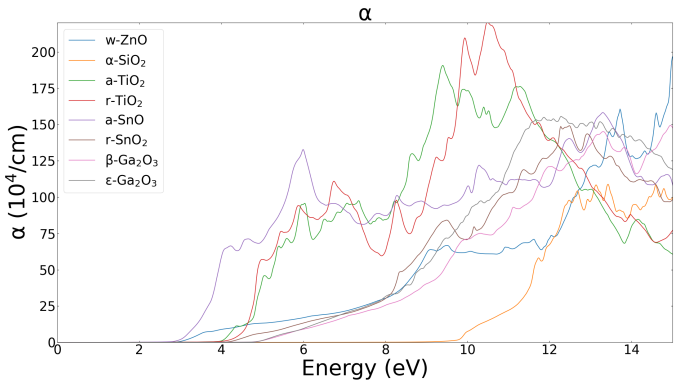

Figure 4.31: The geometric average of absorption coefficient, $\alpha^1 = (\alpha^1_{xx} + \alpha^1_{yy} + \alpha^1_{zz})/3$, for the respective materials considered in this work.

4.4 Brillouin Zone Integration

The purpose of this section is to demonstrate how the DOS and other optical properties are effected by the integration method recommended for calculating the properties of semiconductors. The work presented in this section is performed with PBE calculations. Hence, the DOS and the imaginary dielectric function for r-TiO_2 near the conduction band with respect to the $\boldsymbol{k}$ mesh will be considered closely. The DOS is given by

$$g(E) = 2 \int \frac{d\boldsymbol{k}}{(2\pi)^3} \delta(E - \varepsilon(\boldsymbol{k})). \tag{4.1}$$

The CBM and VBM are located in parabolic bands. The energy for an electron very close to the CBM is expected to be

$$\varepsilon_c = E_g + \frac{\hbar^2 \boldsymbol{k}^2}{2m}, \tag{4.2}$$

where m is the effective mass and $\hbar$ is the Planck constant [19]. Inserting ε_c into Eq. 4.1 and integrating, $g(E)$ is written as

$$g(E) = \frac{\sqrt{2m^3}}{\pi^2 \hbar^3} \sqrt{E}. \tag{4.3}$$

A quadratic function is illustrated in Fig. 4.32. This function simulates how the CBM is expected to look in two dimensions, assuming that the CBM is located at a parabolic band in three dimensions. The trend of linear interpolation is also presented in this figure. This is presented to illustrate the deviation from the quadratic function. The integration method recommended for semiconductors includes linear interpolation, as described in detail in Sect. 2.2.6. The parabolic band is described in terms of a sum of linear functions, rather than a quadratic function, the energy at the conduction band is proportional to the $\boldsymbol{k}$ points rather than the squared $\boldsymbol{k}$ points. Then $\varepsilon \propto \boldsymbol{k}$ and Eq. 4.3 should be rewritten as

$$g(E) \propto E^2, \tag{4.4}$$

in each $\boldsymbol{k}$ point interval.

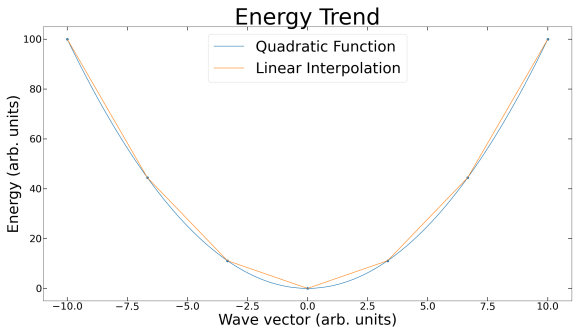

Figure 4.32: The trend of a quadratic function and the linear interpolation between some discrete points in the quadratic function.

In order to illustrate the dependency of the $\boldsymbol{k}$ mesh, DOS calculated with different $\boldsymbol{k}$ meshes are shown in Fig. 4.33. This figure shows how the estimation of DOS centered near the conduction band edge is a better approach to the DOS expected for a parabolic band as the set of $\boldsymbol{k}$ points increases. The derivation resulting from Eq. 4.3 is based on an assumption of a quadratic energy function, resulting in a square root DOS function with respect to the energy. Equation 4.4 on the other hand is based on the knowledge of error due to linear interpolation used in the integration method of the Brillouin zone, hence based on linear energy functions. This results in a DOS proportional to a quadratic function with respect to the energy, rather than a square root function. It is obvious from Fig. 4.33 that the approximation of the DOS calculated with a smaller amount of $\boldsymbol{k}$ points results in a function similar to a quadratic function. To illustrate the difference of trend between a quadratic function and a square root function, an arbitrary quadratic function and an arbitrary square root function are presented in Fig. 4.34 As the number of $\boldsymbol{k}$ points increases, so does the DOS similarity to a square root function, shown in Fig. 4.33. Naturally, a greater number of $\boldsymbol{k}$ points, hence also a smaller step size for the linear interpolation, results in a better estimation. Nevertheless, the graph representing the DOS for $M = 30$ is not as similar to a square root function as it should be, based on the assumption of the proportionality in Eq. 4.4.

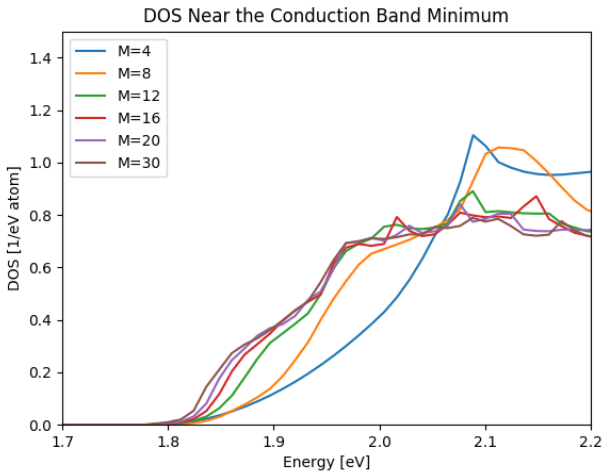

Figure 4.33: The DOS calculated for r-TiO_2, focused at the conduction band edge. The different graphs represent different values of M in $M \times M \times M$ $\boldsymbol{k}$ points.

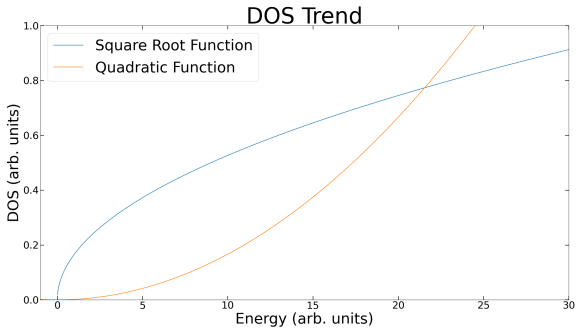

Figure 4.34: The trend of a quadratic function and a square root function, whereas the quadratic function is scaled with a parameter 0.01, with the intention to magnify the difference between the two trends.

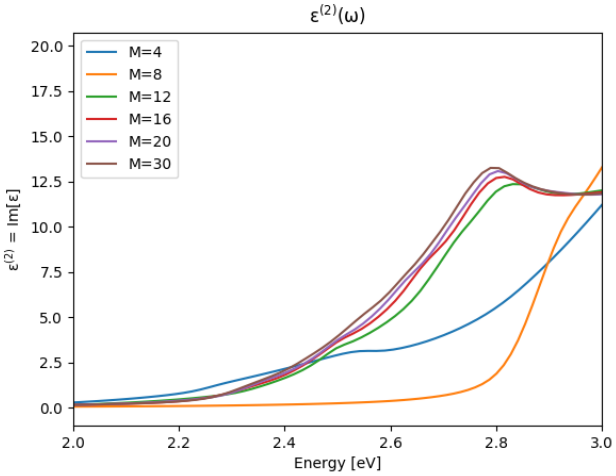

Figure 4.35: The imaginary part of the dielectric function, $\varepsilon^{(2)}$ centered around the CBM for r-TiO_2. The different graphs represent different values of M in $M \times M \times M$ $\boldsymbol{k}$ points.

The dielectric function is as mentioned above very sensitive to the electronic band structure. It can also be directly linked to the effective mass, as shown in Eq. 2.32 in Sect. 2.3.2. It is reasonable to expect flaws near the parabolic bands, due to the tetrahedron method, for this property.

Figure 4.35 reveals that r-TiO_2 shows a stronger electronic response as the number of $\boldsymbol{k}$ points increases. Nevertheless, it is most likely that the lack of density of states has impact for almost all the properties of the material near the CBM. It is reasonable to believe that this might contribute to a small deviation between the polarization and the estimated bandgap value.

It can be concluded that the larger the reciprocal space to be integrated over, the better the approximation. Sadly, this comes at the expense of computational time. The deceptive approximations trending as quadratic functions will result in poorer results of other properties of the material near the conduction band edge, such as the dielectric function and the absorption of the material. However, it is important to notice that the consequential error is small, in the meV region.

The $\boldsymbol{k} \cdot \boldsymbol{p}$ method is reported to provide results using much less computational resources. This computational efficiency could be exploited to use more $\boldsymbol{k}$ points in order to get more accurate calculations near the conduction band edge.

4.5 The $\boldsymbol{k} \cdot \boldsymbol{p}$ Method

With the intention of improving the calculations of semiconductor oxides, the $\boldsymbol{k} \cdot \boldsymbol{p}$ method was implemented in a VASP subroutine. This subroutine is triggered when optical properties are calculated. The ambition was to implement the whole routine in VASP, in order to provide accurate results using less computational resources. The plan was to use the overlap matrix $\boldsymbol{p}$ generated by VASP, but there were some problems regarding this matrix. Eventually a $\boldsymbol{p}$ matrix generated by WIEN2k calculated with the corresponding potential and lattice parameters was used in stead. This was done in order to decide whether it was the program or the VASP $\boldsymbol{p}$-matrix that was the problem. The VASP calculation in combination with the WIEN2k $\boldsymbol{p}$-matrix provided better results.

As described in Sect. 2.2.7, eigenvalues at the reference points $\boldsymbol{k_0}$ are first calculated by using standard methods. Then these eigenvalues are used as basis sets for the calculations of the eigenvalues at $\boldsymbol{k}$ points other than the reference points. The initial idea of this work was to only use one reference point $\boldsymbol{k_0}$, which would be located at the Γ point. The intention was to make a program that performs a Γ point calculation to provide the eigenvalues at the reference point. A Γ point calculation is a calculation with only one $\boldsymbol{k}$ point, namely the Γ point. The initial idea was to start with only one reference point, and then expand to the use of additional reference points if there were any spare time.

In order to get the programming correct, testing was necessary to perform and the chosen material for this testing was r-SnO_2. A good indicator for whether or not the $\boldsymbol{k} \cdot \boldsymbol{p}$ provides sufficient results is the band structure. Hence, the energy levels will be studied in the form of band structures.

In Fig. 4.36 the electronic band structure of r-SnO_2 provided by a regular PBE calculation with a $\boldsymbol{k}$ mesh of $4 \times 4 \times 4$ is presented.

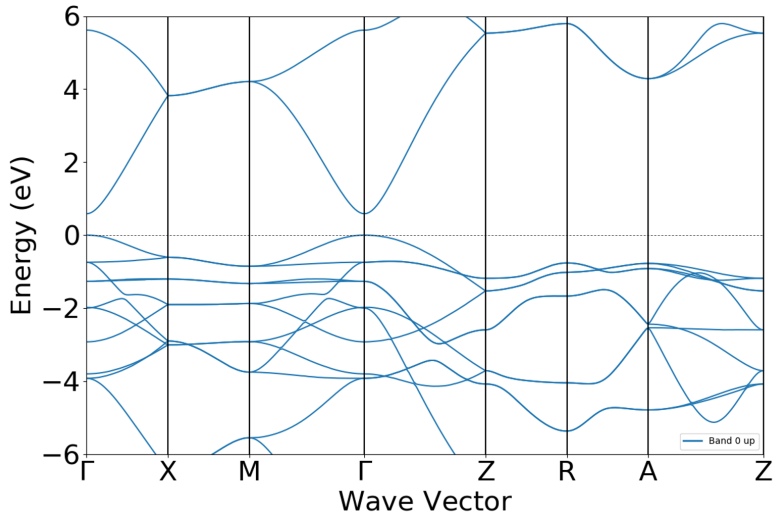

Figure 4.36: The electronic band structure of r-SnO_2 for the path Γ-X-M-Γ-Z-R-A-Z.

The most interesting properties of r-SnO_2 are located around the Γ-point. Therefore, the same calculation was performed along a smaller path, from M-Γ-Z and is presented in Fig. 4.37. This will be the reference structure that the $\boldsymbol{k} \cdot \boldsymbol{p}$ calculated band structures will be compared to.

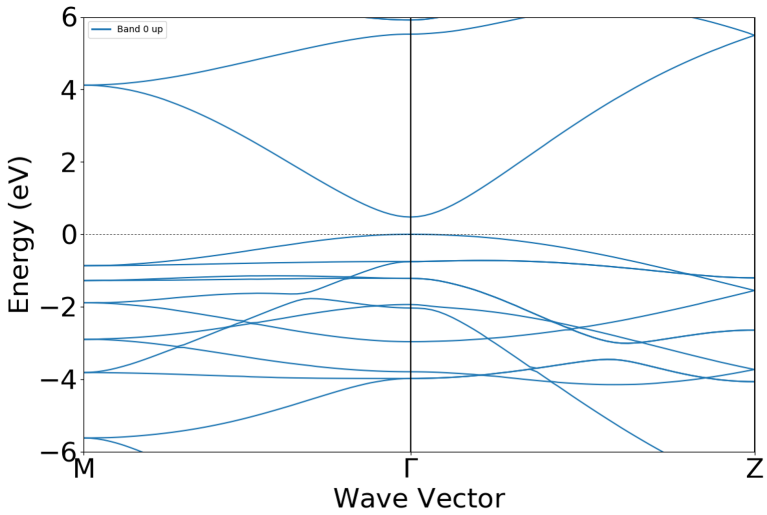

Figure 4.37: The electronic band structure of r-SnO_2 for the path M-Γ-Z.

The $\boldsymbol{k} \cdot \boldsymbol{p}$ with a $\boldsymbol{p}$ matrix generated from WIEN2k provided the band structure presented in Fig. 4.38. At first glance there is one significant deviation compared to Fig. 4.37. The bandgap at the Γ-point is very narrow. Even though PBE calculations provide insufficient bandgap values, the gap presented in Fig. 4.38 is even worse. The energy bands at the Γ point should be more or less located at the same levels as with the standard calculation. The equation for calculating the energies at $\boldsymbol{k}$ points, $E_{\boldsymbol{k}}$, other than at the reference point $\boldsymbol{k_0}$ was presented in the theory Sect. 2.2.7 in Eq. 2.25. At the Γ point $\boldsymbol{k}$ and $\boldsymbol{k_0}$ are the same, therefore, the eigenvalues at this point should be equal to $E_{\boldsymbol{k_0}}$. By further investigation, it is clear that the eigenvalues at the reference point are the source of the problem. As these eigenvalues form the basis for $E_{\boldsymbol{k}}$ calculations, the consequential error becomes severe.

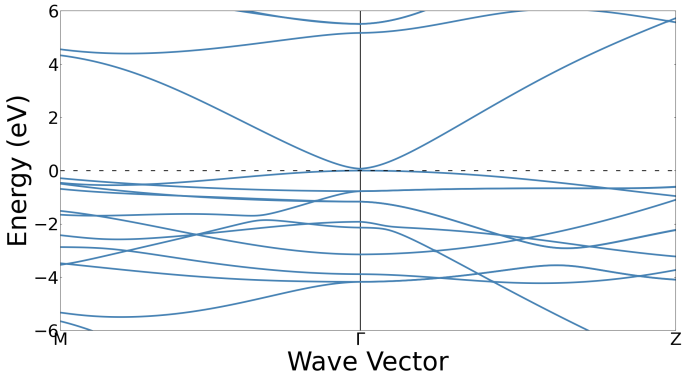

Figure 4.38: The electronic band structure of r-SnO_2 for the path M-Γ-Z.

A standard calculation with a $\boldsymbol{k}$ including more than only one $\boldsymbol{k}$ point provides more accurate Γ point eigenstates than a Γ point calculation does. The accuracy of the numerical method for solving the Brillioiun zone integration increase with an increase of $\boldsymbol{k}$ mesh. That would be the reason for the insufficient values provided by the Γ point calculation. The use of Γ point eigenvalues provided by a standard calculation with a $\boldsymbol{k}$ mesh of $8 \times 8 \times 8$ as the basis set resulted in the band structure presented in Fig. 4.39. These energy levels are in much better agreement with the ones in Fig. 4.37, compared to the energy levels in Fig. 4.38.

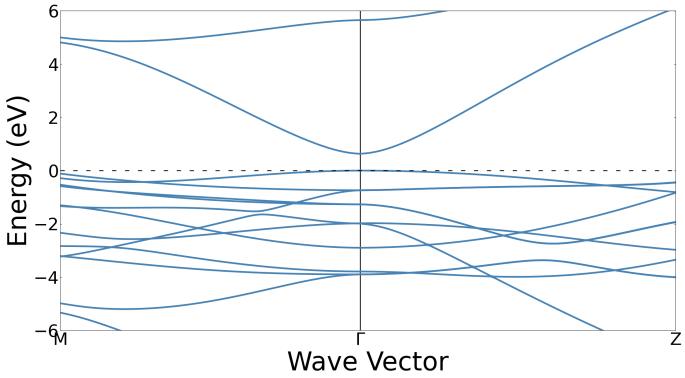

Figure 4.39: The electronic band structure of r-SnO_2 for the path M-Γ-Z.

This demonstrates the importance of accurate eigenstates at the reference point. The idea of using a Γ point calculation to generate the reference point eigenvalues was essentially based on trying to reduce computational time. However, this type of calculation is clearly not sufficient, at least not for this material.

The bandgap energy in the band structure in Fig. 4.39 are similar to the bandgap in the band structure in Fig. 4.37. Hence, it is reasonable to assume that these calculated Γ point eigenvalues are sufficient. By closer examination of the band structure in Fig. 4.39, it is clear that the energy bands at the $\boldsymbol{k}$-points furthest away from the Γ point deviate from energy bands at the same $\boldsymbol{k}$-points in Fig. 4.37. Many of the bands calculated with the $\boldsymbol{k} \cdot \boldsymbol{p}$ method cross with other bands in the location near the M point and the Z point. However, this is not seen in the band structure provided by a regular PBE calculation.

Persson and Ambrosch-Draxl demonstrated in their article, [28], how the eigenvalues calculated at $\boldsymbol{k}$ points closer to the reference point resulted in more accurate results than eigenvalues calculated at $\boldsymbol{k}$ points further from the reference point. They also presented the increasing accuracy of eigenvalues due to increasing number of reference points. This could be the explanation for the crossing of energy bands seen in Fig. 4.39 and not in Fig. 4.37.

Chapter 5

Concluding Remarks

5.1 Conclusion

In this thesis the metal-oxides w-ZnO, α-SiO_2, a-TiO_2, r-TiO_2, a-SnO, r-SnO_2, β-Ga_2O_3, and ε-Ga_2O_3 were considered. Their optical and electronic properties were investigated by using first-principles DFT in conjunction with the Kohn-Sham equation.

In order to improve the accuracy of the calculations, four different approximations to the exchange-correlation functional were considered. For each approximation the lattice parameters a and b and the bandgap energies for the materials evaluated in this work were compared with experimental values. The approximation that provided the overall most accurate results were the hybrid functional with an exchange-correlation energy consisting of 30% HF exchange energy and 70% PBE exchange energy. This hybrid functional approximation was therefore used for the optical and electronic calculations presented in this work. However, not all types of calculations support the use of hybrid functional. Therefore, the calculations of the ionic contribution to the dielectric function had to be performed with PBE calculations. To optimize the accuracy of the calculated static dielectric constants, three different approaches for calculating this were tested. This evaluation made it clear that the ionic contribution is highly dependent on the relaxation of the crystal structure. The conclusion was that a HSE-relaxed structure would provide the best results, compared to the experimental values. In addition to evaluating the static dielectric constants, the high-frequency dielectric constants was also considered with these different approaches. By comparing the high-frequency dielectric constant provided by a PBE calculation and a hybrid functional calculation with experimental values, it was clear that the hybrid functional calculation provides more accurate results than the PBE calculation does. PBE calculations provide poor bandgap energies, while hybrid functional calculations provide bandgap energies that are more consistent with experimental values. Therefore, the superiority of the hybrid functional calculation concerning the high-frequency dielectric constants can be described by the Moss relation, stating that these constants are inversely proportional to the bandgap energy of a material.

The calculated lattice parameters, a, b and c, presented for the materials were in good alignment with the experimental lattice parameters.

Evaluating the calculated bandgap energies, a small deviation from the experimental values were observed. However, the estimation of bandgap energies using the Kohn-Sham approach in DFT is a known challenge and the bandgap energies are much more accurate compared to the PBE calculated bandgap energies, presented in Sect. 3.1. The band structures for all the materials were presented with the corresponding DOS per unit cell. By evaluating the DOS for the different metal-oxides, it was possible to come to a conclusion that it is the O $2p$ orbitals that contributes the most to the VBMs for all the materials.

The calculated dielectric constants had some deviations compared to the experimental values. A trend in underestimating constants was observed for all the materials except for r-TiO_2. A major overestimation was especially seen for the static dielectric constants for r-TiO_2, indicating that its crystal structure is highly sensitive to relaxation. Ionic and electronic polarization were evaluated in the form of dielectric functions. α-SiO_2, β-Ga_2O_3, and ε-Ga_2O_3 showed the strongest magnitude of polarization in the energy range 0 to 0.1 eV, indicating that the ions in these materials are sensitive to the applied electronic fields. Because of the significant amount of phonons in

this region, the materials can absorb infrared radiation in the energy region 0.0 to 0.1 eV. a-SnO and w-ZnO show low absorption coefficients in the visible light energy region. However, this is not significant. Hence, all the materials are expected to be transparent, which is due to their large bandgap energies. All the materials are expected to show absorbance of ultraviolet (UV) radiation. The electronic polarization was also evaluated in light of the bandgap values. For α-SiO_2, r-TiO_2 and r-SnO_2 the responses to an electronic field not in correspondence with the bandgap energies. This indicates that a transition between the VBM and the CBM within each material is forbidden. The same is seen for the indirect bandgaps for a-SnO and a-TiO_2.

How the DOS and other optical properties are effected by the linear tetrahedron method was demonstrated by presenting how the DOS near the CBM for r-TiO_2 are dependent of number of $\boldsymbol{k}$ points. The larger the reciprocal space to be integrated over, the better the approximation, which is known knowledge. However, integrals tend to converge towards their exact solutions and the amount of $\boldsymbol{k}$ points needed to achieve accurate results is usually not severe. It can be concluded that a severe amount of $\boldsymbol{k}$ points is needed to achieve the expected trend of DOS in a material with a CBM of high curvature. This could be important for example in order to achieve highly accurate absorption coefficients near the CBM, or other optical properties near the CBM. However, the error from the linear interpolation is significantly small.

In order to improve the calculations of semiconductor oxides, the $\boldsymbol{k} \cdot \boldsymbol{p}$ method was implemented in a VASP routine. Due to an insufficient momentum matrix $\boldsymbol{p}$ generated by VASP, a momentum matrix $\boldsymbol{p}$ generated by WIEN2k was used instead for the calculations. The $\boldsymbol{k} \cdot \boldsymbol{p}$ calculations were compared to standard PBE calculations in the form of electronic band structures. The initial plan was to use a Γ point calculation to provide the eigenvalues used as the basis set for the $\boldsymbol{k} \cdot \boldsymbol{p}$ calculations, because it is more time efficient. However, the eigenstates provided by a Γ point calculation proved to be highly insufficient. This resulted in a band structure with overlap between the VBM and CBM. A standard calculation with a $\boldsymbol{k}$ mesh of $8 \times 8 \times 8$ provided more accurate eigenstates at the Γ point, compared to the Γ point calculation. The corresponding eigenvalues used as the basis set resulted in a band structure in good agreement with the PBE band structure around the Γ point. A deviation for the energy bands located at the $\boldsymbol{k}$ points furthest away from the Γ point was however observed.

5.2 Further Work

A summary of further investigation regarding the $\boldsymbol{k} \cdot \boldsymbol{p}$ method that would be of interest, includes:

- Expanding the program for calculation of DOS in order to compare the accuracy to a standard PBE calculation generated DOS, with respect to computational time.
- Increasing the number of reference points.
- Implementing a fully developed subroutine for calculating optical and electronic properties with the use of this method.

Further investigations regarding the calculations of optical and electronic properties that would be of interest, includes:

- Calculating the high-frequency dielectric functions with the Bethe-Salpeter equations in order to evaluate if this is a better method for providing results in alignment with experimental values.
- The use of different approximations for the exchange-correlation functional, optimized for each material in order to provide lattice parameters and band gap energies in better alignment with experimental values.
- Convergence tests performed individually for each material, and use the most strict convergence criterion for all the materials.

Bibliography

[1] S. A.Millier, P. Gorai, U. Aydemir, T. O. Mason, V. Stevanovic, E. S. Toberer, and G. J. Snyder. *J. Mater. Chem. C,* **5**, 8854, (2017).

[2] S. M. Antao, I. Hassan, J. Wang, P. L. Lee, and B. H. Toby. *Can. Mineral.* **46**, 4, (2008).

[3] S. M. Antao, I. Hassan, J. Wang, P. L. Lee, and B. H. Toby. *Phys. Solid State* **56**, 2, (2014).

[4] P. Blaha, K. Schwarz, F. Tran, R. Laskowski, G. K. H. Madsen, and L. D. Marks. *J. Chem. Phys.* **152**, 074101, (2020).

[5] P. E. Blöchl, O. Jepsen, and O. K. Andersen. *Phys. Rev. B*, **49**, 23, (1994).

[6] V. E. Bottom. *J. Appl. Phys.* **43**, 4, (1972).

[7] J. Callaway. *Quantum Theory of The Solid State.* (Academic, Boston, 1991).

[8] I. Cora, F. Mezzadri, F. Boschi, M. Bosi, M. Čaplovičová, G. Calestani, I. Dódony, B. Pécz, and R. Fornari. *CrystEngComm* **19**, 11, (2017).

[9] M. Dou and C. Persson. *J. Appl. Phys.*, **113**, 8, (2013).

[10] M. Dresselhaus, G. Dresselhaus, S. B. Cronin, and A. G. S. Filho. *Solid State Properties: From Bulk to Nano.* (Springer, Berlin, 2018).

[11] K. Ellmer, A. Klein, and B. Rech. *Transparent Conductive Zinc Oxide: Basics and Applications in Thin Film Solar Cells.* Springer, Berlin, (2008).

[12] W. Fan, J. Xia, P. Agus, S. Tan, S. Yu, , and X. Sun. *J. Appl. Phys.* **99**, 013702, (2005).

[13] M. Gajdoš, K. Hummer, G. Kresse, J. Furthmüller, and F. Bechstedt. *Phys. Rev. B* **73**, 045112, (2006).

[14] D. J. Griffiths. *Introduction to Quantum Mechanics.* (Cambridge, Cambridge, 2017).

[15] J. Götze and R. Mockel. *Quartz: Deposits, Mineralogy and Analytics.* (Berlin, Springer, 2012).

[16] J. Heyd and G. E. Scuseria. *J. Chem. Phys.* **118**, 8207, (2003).

[17] D. Hu, F. Shen, H. Liu, P. Lu, Y. Lv, D. Liu, and Y. Ma. *Chem.Commun.*, **48**, (2012).

[18] I.Cora, F. Mezzari, F. Boschi, M. Bosi, M. Čaplocičová, G. Calestani, I. Dódony, B. Pécz, and R. Fornari. *CrystEngComm*, **19**, 1509, (2017).

[19] C. Kittel and P. McEuen. *Introduction to Solid State Physics.* (Wiley, Hoboken, 2005).

[20] G. Kresse and J. Furthmüller. *Comput. Mat. Sci.* **6**, 15, (1996).

[21] G. Kresse and J. Furthmüller. *Phys. Rev. B* **54**, 11, (1996).

[22] G. Kresse and J. Hafner. *Phys. Rev. B* **57**, 558, (1993).

[23] A. V. Krukau, O. A. Vydrov, A. F. Izmaylov, and G. E. Scuseria. *J. Chem. Phys.* **125**, 224106, (2006).

[24] P. Mishra, S. Ayaz, T. Srivastava, S.Tiwari, R. Meena, B. Kissinquinker, S. Biring, and S. Sen. *J. Mater. Sci.* **30**, 20, (2019).

[25] M. Mulazzi, F.Reichmann, A. Becker, W. Klesse, P. Alippi, V. Fiorentini, A. Parisini, M. Bosi, and R. Fornari. *Rev. Adv. Mater. Sci.* **44**, 1, (2016).

[26] S. Nagar and S. Chakrabarti. *Optimisation of ZnO Thin Films: Implants, Properties, and Device Fabrication.* Singapore: Springer, (2017).

[27] N. H. Nickel and E. Terukov. *Zinc Oxide - A Material for Micro- and Optoelectronic Applications.* (Dordrecht, Springer, 2005).

[28] C. Persson and C. Ambrosch-Draxl. *Comput. Phys. Commun.* **177**, 3, (2007).

[29] N. Rahimi, R. A. Pax, and E. M. Gray. *Prog. Solid. State Ch.* **44**, 3, (2016).

[30] R. Reddy and Y. N. Ahammed. *Infrared. Phys. Technol.* **36**, 1, (1995).

[31] W. Setyawan and S. Curtarolo. *Comput. Mater. Sci.* **49**, 2, (2010).

[32] T. Shao, S. Liu, and F. Zhang. *Ferroelectrics* **547**, 1, (2017).

[33] D. S. Sholl and J. A. Steckel. *Density Functional Theory.* (Wiley, Hoboken, 2009).

[34] M. Shur. *Solid State Electron.*, **155**, (2019).

[35] G. T. Solola, M. Klopov, J. O. Akinami, T. A. Afolabi, S. Z. Karazhanov, and G. Adebayo. *Mater. Res. Express* **6**, 125915, (2020).

[36] S. Stepanov, V. Nikolaev, V. Bougrouv, and A.E.Romanov. *Rev.Adv.Mater.Sci.*, **44**, 1, (2016).

[37] J. E. N. Swallow, C. Vorwerk, P. Mazzolini, P. Vogt, O. Bierwagen, A. Karg, M. Eickhoff, J. Schörmann, M. R. Wagner, J. W. Roberts, P. R. Chalker, M. J. Smiles, P. Murgatroyd, S. A. Razek, Z. W. Lebens-Higgins, L. F. J. Piper, L. A. H. Jones, P. K. Thakur, T. Lee, J. B. Varley, J. Furthmüller, C. Draxl, T.-D. Veal, and A. Regoutz. *Chem. Mater,* **32**, (19), (2020).

[38] S. M. G. . M. Tripathi. *Sci. Bull.,* **66**, 1639, (2011).

[39] P. Villars and K. Cenzual. *A-TiO2 (TiO2 ana) Crystal Structure: Datasheet from "Pauling File Multinaries Edition, (2012)".*

[40] P. Villars and K. Cenzual. *α-SiO2 (SiO2 rt) Crystal Structure: Datasheet from "Pauling File Multinaries Edition, (2012)".*

[41] P. Villars and K. Cenzual. *β-Ga2O3 (Ga2O3 ht) Crystal Structure: Datasheet from "Pauling File Multinaries Edition, (2012)".*

[42] P. Villars and K. Cenzual. *κ-Ga2O3 (Ga2O3 tf) Crystal Structure: Datasheet from "Pauling File Multinaries Edition, (2012)".*

[43] P. Villars and K. Cenzual. *r-TiO2 (TiO2 rut) Crystal Structure: Datasheet from "Pauling File Multinaries Edition, (2012)".*

[44] P. Villars and K. Cenzual. *SnO Crystal Structure: Datasheet from "Pauling File Multinaries Edition, (2012)".*

[45] P. Villars and K. Cenzual. *SnO2 Crystal Structure: Datasheet from "Pauling File Multinaries Edition, (2012)".*

[46] P. Villars and K. Cenzual. *ZnO Crystal Structure: Datasheet from "Pauling File Multinaries Edition, (2012)".*